

**DESIGN AND CONTROL OF A
MAGNETIC DIPOLE SOURCE
FOR NONCONTACT
MANIPULATION**

by

Andrew J. Petruska

A dissertation submitted to the faculty of
The University of Utah
in partial fulfillment of the requirements for the degree of

Doctor of Philosophy

Department of Mechanical Engineering

The University of Utah

December 2014

Copyright © Andrew J. Petruska 2014

All Rights Reserved

The University of Utah Graduate School

STATEMENT OF DISSERTATION APPROVAL

The dissertation of Andrew J. Petruska
has been approved by the following supervisory committee members:

<u>Jake J. Abbott</u>	, Chair	<u>27 February 2014</u> <small>Date Approved</small>
-----------------------	---------	---

<u>Christoph Boehme</u>	, Member	<u>27 February 2014</u> <small>Date Approved</small>
-------------------------	----------	---

<u>John Hollerbach</u>	, Member	<u>10 March 2014</u> <small>Date Approved</small>
------------------------	----------	--

<u>Gianluca Lazzi</u>	, Member	<u>27 February 2014</u> <small>Date Approved</small>
-----------------------	----------	---

<u>Sanford Meek</u>	, Member	<u>27 February 2014</u> <small>Date Approved</small>
---------------------	----------	---

and by Tim Ameel, Chair/Dean of
the Department/College/School of Mechanical Engineering

and by David B. Kieda, Dean of The Graduate School.

ABSTRACT

This dissertation explores the design and use of an electromagnetic manipulation system that has been optimized for the dipole-field model. This system can be used for noncontact manipulation of adjacent magnetic tools and combines the field strength control of current electromagnetic systems with the analytical modeling of permanent-magnet systems. To design such a system, it is first necessary to characterize how the shape of the field source affects the shape of the magnetic field.

The magnetic field generated by permanent magnets and electromagnets can be modeled, far from the source, using a multipole expansion. The error associated with the multipole expansion is quantified, and it is shown that, as long as the point of interest is 1.5 radii of the smallest sphere that can fully contain the magnetic source, the full expansion will have less than 1% error. If only the dipole term, the first term in the expansion, is used, then the error is minimized for cylindrical shapes with a diameter-to-length ratio of $\sqrt{4/3}$ and for rectangular-bars with a cube.

Applying the multipole expansion to electromagnets, an omnidirectional electromagnet, comprising three orthogonal solenoids and a spherical core, is designed that has minimal dipole-field error and equal strength in all directions. Although this magnet can be constructed with any size core, the optimal design contains a spherical core with a diameter that is 60% of the outer dimension of the magnet. The resulting magnet's ability to dextrously control the field at a point is demonstrated by rotating an endoscopic-pill mockup to drive it through a lumen and roll a permanent-magnet ball through several trajectories. Dipole fields also apply forces on adjacent magnetized objects. The ability to control these forces is demonstrated by performing position control on an orientation-constrained magnetic float and finally by steering a permanent magnet, which is aligned with the applied dipole field, around a rose curve.

CONTENTS

ABSTRACT	iii
LIST OF FIGURES	vi
CHAPTERS	
1. INTRODUCTION	1
1.1 References	3
2. OPTIMAL PERMANENT-MAGNET GEOMETRIES FOR DIPOLE FIELD APPROXIMATION	5
2.1 Introduction	6
2.2 Permanent-Magnet Field Approximation	7
2.3 Magnet Multipole Expansion	8
2.3.1 Cylindrical Magnet	8
2.3.2 Rectangular-Cross-Section Bar Magnet	9
2.3.3 Validation of Multipole Expansions With FEA Solutions	10
2.4 Optimal Geometric Relations for Dipole Approximation	10
2.4.1 Cylinders	10
2.4.2 Rectangular-Cross-Section Bar	11
2.4.3 Axially Magnetized Washer	11
2.4.4 Diametrically Magnetized Washer	11
2.5 Error Characterization of Optimal Dipole Geometries	12
2.6 Conclusion	13
2.7 References	13
3. OMNIMAGNET: AN OMNIDIRECTIONAL ELECTROMAGNET FOR CONTROLLED DIPOLE-FIELD GENERATION	15
3.1 Introduction	16
3.2 Design and Optimization	17
3.2.1 Solenoid Multipole Field Expansion	17
3.2.2 Core Dipole-Field Contribution	18
3.2.3 Dipole Moment Equalization	18
3.2.4 Prototype	19
3.3 Effect of Adjacent Magnetic Sources	20
3.4 Physical Properties	20
3.4.1 Weight	21
3.4.2 Resistance and Heating/Cooling Limits	21
3.4.3 Inductance and Time Constant	21
3.5 Field Control	21
3.6 Remote Manipulation with an Omnimagnet	22

3.7	Discussion	22
3.8	Conclusions	22
3.9	Appendix	23
3.10	Acknowledgment	24
3.11	References	24
4.	REMOTE MANIPULATION WITH A STATIONARY COMPUTER-CONTROLLED MAGNETIC DIPOLE SOURCE	26
4.1	Introduction	27
4.2	Magnetics Background	27
4.3	Field Control	27
4.4	Torque Control	28
4.5	Force Control	28
4.6	Field-Aligned Force Control	29
4.7	Comment on Reflective Force and Torque	31
4.8	Conclusion	31
4.9	References	31
5.	RECOMMENDATIONS FOR FUTURE WORK	33
5.1	References	36
6.	CONCLUSIONS	37

LIST OF FIGURES

2.1 Geometry definition for cylindrical magnets.	8
2.2 Definition of a rectangular-cross-section bar magnet geometry.	9
2.3 Contour plot showing the 2% (outer) and 50% (inner) bands of error between the multipole expansion and the FEA model for several geometries of cylinder and rectangular magnets.	10
2.4 The average error of the first nine terms of the multipole approximation as compared to FEA simulation over a spherical surface as a function of distance for several different geometries of cylinder and rectangular magnets.	11
2.5 Definition of washer-shaped magnet geometry.	12
2.6 The average errors associated with different geometries of cylindrical and rectangular permanent magnets are plotted as a function of distance from the center of the magnet.	12
2.7 The error associated with the optimal dipole geometries.	12
2.8 Variation in dipole approximation error as a function of angle for an axially magnetized cylindrical magnet with $\beta = \sqrt{4/3}$	13
2.9 Variation in dipole approximation error as a function of angle for an optimal diametrically magnetized cylindrical magnet and cube magnet.	13
3.1 The assembled Omnimagnet forms a cube constructed of three nested orthogonal solenoids surrounding a spherical core of ferromagnetic material.	16
3.2 The optimal geometry for a no-quadrupole Omnimagnet.	19
3.3 The assembled Omnimagnet used in the testing described in this paper.	19
3.4 The field shape (top, dotted) and magnitude (top, solid and color contour), and field error relative to the dipole approximation (bottom) are shown.	20
3.5 Propulsion of a helical capsule at $10 \text{ mm} \cdot \text{s}^{-1}$ through a lumen located 120 mm from the surface of the Omnimagnet, which is applying a rotating magnetic field at the location of the helical capsule.	23
4.1 Position control of a spherical magnet using a rotating field to direct the rolling direction of the ball.	29
4.2 Position servo control of a floating magnet using applied force, generated by an Omnimagnet.	29
4.3 Manipulability measure of a tool aligned with a source's dipole field as a function of angular position inside of the 28° conic workspace.	30

4.4 Semiboyant capsule is levitated and position controlled about a rose curve using a field-aligned force control approach.	31
---	----

CHAPTER 1

INTRODUCTION

Manipulation of objects typically requires physical contact between the manipulator and the object to achieve a desired force or torque transfer. This physical connection is a limiting factor when control of objects is desired in areas with access restrictions such as surgery, where the larger the access incision the longer the recovery time and greater the cost. Magnetic fields provide a method of applying forces and torques to an adjacent object without a mechanical connection. Unfortunately, Earnshaw's theorem proves that no stable equilibrium can exist in a system comprising solely static magnetic elements [1]. The instability has been exploited over the past 100 years to control objects using magnetic field sources with initial examples including the removal of ferrous objects from wounds during the first and second world wars [2]. Computer-controlled magnetic manipulation, which can stabilize the magnetic interactions through feedback and time-varying fields, was explored some 80 years later when IBM investigated the use of magnetics to create a spherical robotic wrist [3], the University of Texas at Austin applied magnetic levitation technologies to micro-robotic control [4], and the University of Virginia began using air-core solenoids to control ferromagnetic objects in the brain for stereotactic surgery [5].

Currently, the state of the art for electromagnet manipulation has split into two main areas: the uniform-direction and uniform-gradient fields produced by MRI machines and similar laboratory setups are used to control devices for medical applications [6], and the nonlinear fields generated by collections of electromagnets that have been calibrated *in situ* are used for position and orientation control of both soft-magnetic objects and permanent magnets [7], [8]. These two approaches rely on an accurate model of the system's field for control; this accuracy is obtained either through design to achieve uniformity (e.g., MRI systems) or calibration to empirically quantify the response (e.g., solenoid based systems) *in situ*.

Permanent magnet based systems, which require no electrical power to generate a strong static field, have been used for pulling and rolling tasks in which the environment provides some structure [9]–[13], as well as for quasistatic pointing tasks of tethered devices such as magnetic catheters [14]. The magnetic field is generally modeled by the dipole-field model since the operating distances are large relative to the size of the magnet. Control of adjacent objects is then converted to position and orientation control of the magnetic source to achieve a desired response given the dipole-field model. As these systems typically are unable to change the location and orientation of the source magnet faster than the end effector can respond, a nonmagnetic force (e.g., gravity) is required to stabilize the instability predicted by Earnshaw.

An electromagnet capable of producing a magnetic moment with a variable strength and orientation will provide the field strength control associated with traditional electromagnet systems and the adjacent and adaptable workspace associated with permanent-magnet systems. To create such a device, it is necessary to surround a ferromagnetic core with at least three linearly independent (e.g., orthogonal) solenoids. The concept of using three orthogonal solenoids to generate a magnetic field is not new, as it has been explored as a method of magnetic localization [15], inductive power coupling [16], and multi-object formation flight [17] and is the fundamental basis for MRI machines and Helmholtz coils. However, neither using three orthogonal solenoids for adjacent magnetic manipulation (i.e., external to the enclosed volume of the electromagnets), nor using three orthogonal solenoids with an internal spherical core has been explored previously.

The development of a controllable dipole-source for manipulation can be split into three main tasks. First, understand the shape of the magnetic fields produced by different source geometries with similar magnetic moments. Second, use the knowledge of how geometry affects field shape to design an optimized controllable dipole-source. And, third, determine the capabilities and limitations of this device for control.

The magnetic field associated with either a current distribution or a material magnetization can be approximated using an infinite series—the multipole expansion. This expansion is only accurate for distances outside of a sphere that bounds all of the magnetized material and current. The first nonzero term in this expansion is the dipole-field term [18]:

$$\mathbf{B} = \frac{\mu_0}{4\pi\|\mathbf{p}\|^3} \left(3\hat{\mathbf{p}}\hat{\mathbf{p}}^\top - \mathbb{I} \right) \mathbf{m}, \quad (1.1)$$

which is convenient for control because the resulting field \mathbf{B} is linear with respect to the source’s dipole moment \mathbf{m} at the location \mathbf{p} , where $\|\mathbf{p}\|$ is the euclidian length of the vector from the source to the point of interest and $\hat{\mathbf{p}}$ is its unit-length direction, \mathbb{I} is a 3×3 identity

matrix, and μ_0 is the permeability of free space. The higher-order terms in the multipole expansion are not linear with respect to dipole moment and are more difficult to use in an inverse solution for field or field gradient. Thus, it is desirable to choose a magnetic field source that is well modeled by the dipole term alone. Chapter 2 discusses how to accomplish this with a permeant magnet system and Chapter 3 applies the same technique to an electromagnet system.

The dipole moment of a system is a function of the size of that system [18]:

$$\mathbf{m} = \iiint_{\mathcal{V}} (\mathbf{M}(\mathbf{r}) + \frac{1}{2}\mathbf{r} \times \mathbf{J}(\mathbf{r})) d\mathcal{V}, \quad (1.2)$$

where \mathcal{V} represents the volume of the source, $\mathbf{M}(\mathbf{r})$ is the magnetization of any integral material, $\mathbf{J}(\mathbf{r})$ is the current density present, and \mathbf{r} is the displacement vector from the reference center to the point of integration. The magnetization $\mathbf{M}(\mathbf{r})$ is also a linear function of the applied current density \mathbf{J} , and in systems with ferromagnetic materials can account for a large percentage of the system's dipole-moment. To design an electromagnet system that is well modeled by a dipole-field, it is necessary to account for both the current contribution and the magnetization contribution to the magnetic field. Chapter 3 analyzes how to construct an electromagnetic system, which is optimized for strength, that has the same dipole-moment strength for an applied current vector in any direction.

Chapter 4 examines how to use such a device to control adjacent permanent magnet tools. Since a single source has only three degrees of freedom (the three solenoid currents), it is shown that it is not possible to independently control torque and force on an object. Despite this limitation, it is still possible to dexterously manipulate an object by operating in situations where the forces cause minimal disturbances, the torques can be resolved by external support, or the tool's orientation is free to align with the applied field.

Finally, some recommendations for future work are provided based on the lessons learned from this effort.

1.1 References

- [1] S. Earnshaw, "On the nature of the molecular forces which regulate the constitution of the luminiferous ether," *Trans. Camb. Phil. Soc.*, vol. 7, pp. 97–112, 1842.
- [2] F. Kammerer, "Transactions of the New York surgical society: stated meeting, held october 13, 1915," *Ann. of Surgery*, vol. 63, no. 1, pp. 111–126, 1916.
- [3] R. Hollis, S. Salcudean, and A. Allan, "A six-degree-of-freedom magnetically levitated variable compliance fine-motion wrist: design, modeling, and control," *IEEE Trans. Robotics and Automation*, vol. 7, no. 3, pp. 320–332, 1991.

- [4] R. E. Pelrine, “Magnetically levitated micro-robotics,” PhD thesis, University of Texas at Austin, 1988.
- [5] M. Grady, M. Howard III, J. Molloy, R. Ritter, E. Quate, and G. Gillies, “Nonlinear magnetic stereotaxis: three-dimensional, in vivo remote magnetic manipulation of a small object in canine brain,” *Med. Phys.*, vol. 17, p. 405, 1990.
- [6] J. B. Mathieu, G. Beaudoin, and S. Martel, “Method of propulsion of a ferromagnetic core in the cardiovascular system through magnetic gradients generated by an mri system,” *IEEE Trans. Bio-Med. Eng.*, vol. 53, no. 2, pp. 292–299, 2006.
- [7] M. P. Kummer, J. J. Abbott, B. E. Kratochvil, R. Borer, A. Sengul, and B. J. Nelson, “OctoMag: an electromagnetic system for 5-DOF wireless micromanipulation,” *IEEE Trans. Robot.*, vol. 26, no. 6, pp. 1006–1017, 2010.
- [8] P. Berkelman and M. Dzadovsky, “Magnetic levitation over large translation and rotation ranges in all directions,” *IEEE/ASME Trans. Mechatronics*, vol. 18, no. 1, pp. 44–52, 2013.
- [9] M. H. Hagiwara, T. K. Kawahara, Y. Yamanishi, and F. Arai, “Driving method of microtool by horizontally arranged permanent magnets for single cell manipulation,” *Appl. Phys. Lett.*, vol. 97, no. 013701, pp. 1–3, 2010.
- [10] G. Ciuti, P. Valdastri, A. Menciassi, and P. Dario, “Robotic magnetic steering and locomotion of capsule endoscope for diagnostic and surgical endoluminal procedures,” *Robotica*, vol. 28, no. Special Issue 02, pp. 199–207, 2010.
- [11] S. Yim and M. Sitti, “Design and rolling locomotion of a magnetically actuated soft capsule endoscope,” *IEEE Trans. Robot.*, vol. 28, no. 1, pp. 183–194, 2012.
- [12] A. W. Mahoney, D. L. Cowan, K. M. Miller, and J. J. Abbott, “Control of untethered magnetically actuated tools using a rotating permanent magnet in any position,” in *IEEE Int. Conf. Robotics and Automation*, 2012, pp. 3375–3380.
- [13] A. W. Mahoney and J. J. Abbott, “5-DOF manipulation of a magnetic capsule in fluid using a single permanent magnet: proof-of-concept for stomach endoscopy,” *Hamlyn Symp. Medical Robotics*, 2013.
- [14] M. N. Faddis, W. Blume, J. Finney, A. Hall, J. Rauch, J. Sell, K. T. Bae, M. Talcott, and B. Lindsay, “Novel, magnetically guided catheter for endocardial mapping and radiofrequency catheter ablation,” *Circulation*, vol. 106, pp. 2980–2985, 2002.
- [15] F. Raab, E. Blood, T. Steiner, and H. Jones, “Magnetic position and orientation tracking system,” *IEEE Tran. Aero. and Elec. Sys.*, vol. AES-15, no. 5, pp. 709–718, 1979.
- [16] R. Carta, J. Thoné, and R. Puers, “A wireless power supply system for robotic capsular endoscopes,” *Sens. Actuators, A*, vol. 162, no. 2, pp. 177–183, 2010.
- [17] R. J. Sedwick and S. A. Schweighart, “Electromagnetic formation flight,” *Advances in the Astronautical Sciences*, vol. 113, pp. 71–83, 2003.
- [18] D. J. Griffiths, *Introduction to Electrodynamics*. Upper Saddle River, NJ: Prentice Hall, 1999.

CHAPTER 2

OPTIMAL PERMANENT-MAGNET GEOMETRIES FOR DIPOLE FIELD APPROXIMATION

The following paper, originally published in IEEE Transactions on Magnetics and reprinted with permission, is aimed at understanding how well the dipole-field model predicts the magnetic field associated with several different permanent magnet shapes. The paper then determines what the optimal geometric aspect ratios are for several shapes to be represented by a dipole field.

A. J. Petruska and J. J. Abbott, "Optimal permanent-magnet geometries for dipole field approximation," *IEEE Trans. Magn.*, vol. 49, no. 2, pp. 811–819, 2013

©2013 IEEE. Personal use of this material is permitted. Permission from IEEE must be obtained for all other uses, in any current or future media, including reprinting/republishing this material for advertising or promotional purposes, creating new collective works, for resale or redistribution to servers or lists, or reuse of any copyrighted component of this work in other works.

Optimal Permanent-Magnet Geometries for Dipole Field Approximation

Andrew J. Petruska and Jake J. Abbott

Department of Mechanical Engineering, University of Utah, Salt Lake City, UT 84112 USA

The dipole approximation for magnetic fields has become a common simplifying assumption in magnetic-manipulation research when dealing with permanent magnets because the approximation provides convenient analytical properties that are a good fit at large distances. What is meant by “good fit at large distances” is generally not quantified in the literature. By using a parameterized multipole expansion and collaborating finite-element analysis (FEA) simulations to represent the magnet’s field, we quantify the error associated with the dipole approximation as a function of distance from the permanent magnet. Using this expression, we find cylindrical, washer, and rectangular-cross-section bar permanent-magnet aspect ratios that minimize the error of the dipole approximation. For cylinders and rectangular-cross-section bars, these aspect ratios are a diameter-to-length ratio of $\sqrt{4/3}$ and a cube, respectively.

Index Terms—Magnetic analysis, magnetostatics, permanent magnets.

I. INTRODUCTION

THE magnetic fields generated by current distributions and permanent magnet can be modeled in numerous ways from direct integration of the Biot–Savart law, to finite-element analysis (FEA), to harmonic expansions of the fields. The dipole approximation, the first spherical harmonic of the field, provides a concise and easily manipulated representation of the magnetic field and is increasingly accurate with distance. This approximation is commonly used for localization of objects in areas ranging from medical imaging applications [1], to military applications [2]–[4], to object tracking [5]–[20]. The dipole representation also provides interesting applications in real-time control of magnetic devices for medical applications [21]–[24]. A pure dipole field can be generated by a uniformly magnetized spherical permanent magnet; however, other shapes of permanent magnets can be represented by a dipole field as an approximation at large distances. Understanding the limitations of this approximation for the commonly available cylindrical, washer, and rectangular-cross-section bar permanent magnets is the focus of this paper, along with answering the question: “What shape of cylindrical/washer/bar permanent magnet is best represented by a pure dipole field?”

There are works that explicitly address the accuracy of the dipole approximations of permanent magnets. Hu *et al.* [6]–[9] propose placing a cylindrical permanent magnet inside a capsule endoscope for localization. They use the dipole approximation to describe the magnetic field produced by the permanent magnet and use linear calibration techniques to minimize the error associated with the strength of the magnet. Wang and Meng [11] explore the accuracy of the dipole model for two types of cylindrical magnets for use as magnetic markers in capsule endoscopes. They quantify the error along the axis and radius of the cylindrical magnet and suggest a rectangular “keep-out region” for the approximation that is three times the dimension of the magnet, but they do not examine the error associated with the model for other locations. They also indicate that

an axially magnetized magnet with a diameter-to-length ratio of 2.5 is better represented by the dipole model than an axially magnetized magnet with a diameter-to-length ratio of 0.5. Fountain *et al.* [21] examine the use of a rotating permanent magnet to control helical swimmers and propose using a dipole model to represent the field of the cylindrical permanent magnets. The approximation is justified *a posteriori* by a least squares fit of the dipole model to experimental data collected along the magnetization axis for both diametrically magnetized and axially magnetized cylindrical magnets. Interestingly, the fit to the diametric magnet shows better agreement with the dipole model than the axial magnet with the same geometry. Mahoney *et al.* [23] continued this research and exploited the linear-algebraic properties of the dipole field to show interesting force and torque combinations can be applied by one rotating permanent magnet acting on another sympathetically rotating permanent magnet. They then use the dipole model to demonstrate that rotating magnetic fields can be generated about arbitrary axes in space using a single rotating permanent magnet in any relative position [24]. The above works show the dipole model is an accurate approximation for distances far away from the permanent magnet and imply that using a permanent magnet that is more accurately modeled by the dipole approximation at distances nearer to the magnet will enable more accurate real-time magnetic control of untethered devices. Two observations in the works by Fountain *et al.* and by Wang and Meng indicate there may be an optimal aspect ratio and magnetization direction to accurately represent the magnetic field produced by a cylindrical permanent magnet using the dipole approximation.

To explore the nature of a shape that is optimally represented by the dipole-model approximation and to quantify the error in the model at any location outside the magnet, a parameterized multipole expansion is presented in this paper for axially and diametrically magnetized cylindrical magnets and rectangular-cross-section bar magnets. The accuracy of this expansion is verified by comparisons to FEA models of the magnetic fields from different magnet geometries. Since the dipole approximation is the first term of this expansion, analytically calculating the optimal shape aspect ratios can be achieved by minimizing the contribution of the remaining terms to the field representation.

The paper is structured as follows. First, the theoretical foundation for a multipole expansion for representing the magnetic

Manuscript received April 12, 2012; revised June 05, 2012; accepted June 07, 2012. Date of publication June 18, 2012; date of current version January 22, 2013. Corresponding author: A. J. Petruska (e-mail: Andrew.Petruska@utah.edu.).

Color versions of one or more of the figures in this paper are available online at <http://ieeexplore.ieee.org>.

Digital Object Identifier 10.1109/TMAG.2012.2205014

field of a permanent magnet is reviewed, and the criteria for defining the shape with minimal dipole-model error will be introduced. Then, the multipole expansion for axially and diametrically magnetized cylindrical magnets and rectangular-cross-section bar magnets is solved and compared to FEA models of several different magnet geometries to validate the expansion. The optimal aspect ratios for cylindrical magnets and rectangular bars is then solved and extended to washers. Finally, the error associated with the dipole approximation for both the optimal and other commonly available shapes is presented.

II. PERMANENT-MAGNET FIELD APPROXIMATION

The magnetization \mathbf{M} inside a permanent magnet is a function of the applied field \mathbf{H}_a , the magnetic remanence of the material \mathbf{H}_r , the susceptibility of the material χ , and the shape demagnetization factors along the principal axes of the magnet N_i

$$\mathbf{M} = \begin{bmatrix} \frac{1}{1 + \chi N_1} & 0 & 0 \\ 0 & \frac{1}{1 + \chi N_2} & 0 \\ 0 & 0 & \frac{1}{1 + \chi N_3} \end{bmatrix} (\chi \mathbf{H}_a + \mathbf{H}_r) \quad (1)$$

where all vectors are expressed relative to the principal axes of the magnet. The demagnetization factors are a set of three fractional values, which sum to one, that describe how a given shape magnetically interacts with itself, and how susceptible the shape is to magnetization in each of the principle directions; for a sphere, the demagnetization factors are 1/3 in each principle direction. The demagnetization factors for ellipsoids of revolution, cylinders with ellipsoidal cross sections, and rectangular bars have been calculated [25]–[28]. For hard-magnetic materials with relatively low magnetic recoil susceptibilities for applied fields weaker than the coercive field strength, such as NdFeB with $\chi \approx 0.05$, the demagnetizing field becomes negligible and the magnetization reduces to the magnetic remanence of the material. For a permanent magnet with no external field applied, the magnetic \mathbf{H} field can be described as the gradient of a scalar potential Φ , which can be defined by the magnetization of the object [29]

$$\mathbf{H} = -\nabla \Phi, \quad \nabla^2 \Phi = \nabla \cdot \mathbf{M}. \quad (2)$$

This can be solved using direct integration [29]

$$\Phi(\mathbf{p}) = \frac{1}{4\pi} \left(\int_V \frac{\nabla \cdot \mathbf{M}}{|\mathbf{p} - \boldsymbol{\rho}|} dv + \oint_S \frac{\hat{\mathbf{n}} \cdot \mathbf{M}}{|\mathbf{p} - \boldsymbol{\rho}|} da \right) \quad (3)$$

where \mathbf{M} is the magnetization, $\hat{\mathbf{n}}$ is the normal unit vector pointing out of the surface of the magnetized material, \mathbf{p} is the vector from the center of the magnetized volume to the point of interest and is independent of the integral, $\boldsymbol{\rho}$ is the vector from the center of the magnetized volume to the point of integration, and $\hat{\mathbf{p}}$ and $\hat{\boldsymbol{\rho}}$ are their respective unit vectors.

For permanent magnets with low susceptibilities and uniform remanence, which is a reasonable assumption for permanent

magnets that are saturated during manufacturing, the divergence in the volume ($\nabla \cdot \mathbf{M}$) is equal to zero, reducing (3) to

$$\Phi(\mathbf{p}) = \frac{1}{4\pi} \oint_S \frac{\hat{\mathbf{n}} \cdot \mathbf{M}}{|\mathbf{p} - \boldsymbol{\rho}|} da. \quad (4)$$

This can be rewritten using a Taylor series as a multipole expansion if the points of interest are outside the minimum bounding sphere (i.e., the smallest sphere that will encompass the magnet) surrounding the permanent magnet [30]

$$\Phi(\mathbf{p}) = \frac{1}{4\pi} \sum_{n=0}^{\infty} \frac{1}{p^{n+1}} \oint_S \rho^n P_n(\hat{\mathbf{p}} \cdot \hat{\boldsymbol{\rho}}) (\hat{\mathbf{n}} \cdot \mathbf{M}) da \quad (5)$$

where $P_n()$ are Legendre polynomials $p = |\mathbf{p}|$ and $\rho = |\boldsymbol{\rho}|$. The magnetic field represented by this scalar potential is only defined outside the permanent magnet and is

$$\mathbf{B} = \mu \mathbf{H} = -\mu \nabla \Phi \quad (6)$$

where μ is the permeability of the surrounding medium (for free space $\mu = \mu_0 \equiv 4\pi \times 10^{-7} \text{ N} \cdot \text{A}^{-2}$).

As a consequence of $\nabla \cdot \mathbf{B} = 0$, no even terms (e.g., $\propto 1/p^2, \propto 1/p^4, \dots$) exist in (6). The first nonzero term of the expansion is the dipole term ($\propto 1/p^3$), which is independent of geometry and is commonly used for approximation of the magnetic field for control applications because of its convenient vector form. This term is

$$\mathbf{B}_{\text{dipole}}(\mathbf{p}) = \frac{\mu_0}{4\pi} \frac{1}{p^3} (3\hat{\mathbf{p}}\hat{\mathbf{p}}^T - \mathbf{I}) \mathbf{m} \quad (7)$$

where \mathbf{I} is a 3×3 identity matrix and \mathbf{m} is being introduced here as the dipole moment of the object defined by

$$\mathbf{m} \equiv \int_V \mathbf{M} dv. \quad (8)$$

The next nonzero term in the series is the quadrupole term ($\propto 1/p^5$) and the next is a hexapole ($\propto 1/p^7$), all of which are functions of magnet geometry. In these higher order terms, β will represent any factors that parameterize the shape of the magnet, such as a diameter-to-length ratio for a cylinder.

For an approximation of the field consisting of the first T terms, the relative error at any given point is

$$\begin{aligned} \text{Error}(\mathbf{p}, \beta) &\equiv \frac{|\mathbf{B}_{\text{actual}} - \mathbf{B}_{\text{approx}}|}{|\mathbf{B}_{\text{actual}}|} \\ &= \frac{\left| \mathbf{B}_{T+1}(\mathbf{p}, \beta) + \mathbf{B}_{T+2}(\mathbf{p}, \beta) + \sum_{n=T+3}^{\infty} \mathbf{B}_n(\mathbf{p}, \beta) \right|}{\left| \sum_{n=1}^{\infty} \mathbf{B}_n(\mathbf{p}, \beta) \right|}. \end{aligned} \quad (9)$$

Without loss of generality, T will be assumed to be an odd number, requiring the even terms (\mathbf{B}_{T+1} and \mathbf{B}_{T+3}) to be zero, simplifying the error to

$$\text{Error}(\mathbf{p}, \beta) = \frac{\left| \mathbf{B}_{T+2}(\mathbf{p}, \beta) + \sum_{n=T+4}^{\infty} \mathbf{B}_n(\mathbf{p}, \beta) \right|}{\left| \sum_{n=1}^{\infty} \mathbf{B}_n(\mathbf{p}, \beta) \right|}. \quad (10)$$

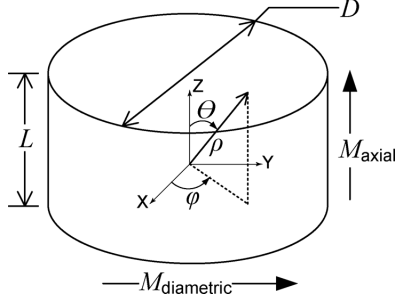


Fig. 1. Geometry definition for cylindrical magnets. The spherical coordinate definition is shown for the axially magnetized case only.

As \mathbf{B}_{T+4} and higher order terms are asymptotically bounded by the \mathbf{B}_{T+2} term, the optimal approximation geometry for distances much greater than the radius of the minimum bounding sphere radius R_s can be determined by minimizing the magnitude of the \mathbf{B}_{T+2} term alone. As this provides the optimal geometry for distances far away from the minimum bounding sphere, it is conceivable that at some intermediate distance a different geometry could provide a locally optimal solution. To determine locally optimal solutions, the integral of (10) over the region of interest would need to be minimized and more terms than just the \mathbf{B}_{T+2} term would need to be considered. As this minimization is application specific, only the far-field optimal geometry for the dipole approximation ($T = 1$) will be considered in this paper and the quadrupole term \mathbf{B}_3 term will be minimized by finding the value of β that sets the contribution of the \mathbf{B}_3 term to zero at every location in space.

III. MAGNET MULTIPOLE EXPANSION

A. Cylindrical Magnet

Cylindrical permanent magnets are most readily available in the axially magnetized and diametrically magnetized forms. Without loss of generality, the axis of the cylinder is aligned with the Cartesian z -axis, as shown in Fig. 1. The parameter that characterizes the shape of the cylinder is the diameter-to-length aspect ratio β . The following equations summarize some useful relationships using this parametrization, where R_s is the radius of the minimum bounding sphere and V is the volume of the cylinder:

$$\beta \equiv \frac{D}{L} \quad R_s = \left(\frac{V}{2\pi} \right)^{\frac{1}{3}} \frac{\sqrt{\beta^2 + 1}}{\beta^{\frac{2}{3}}} \quad (11)$$

$$D = 2 \left(\frac{V\beta}{2\pi} \right)^{\frac{1}{3}} \quad L = 2 \left(\frac{V}{2\pi\beta^2} \right)^{\frac{1}{3}}.$$

For materials like NdFeB with small susceptibilities ($|\chi| \ll 1$), (1) and (8) simplify to $\mathbf{m} \approx \mathbf{H}_r V$, which, given a minimum bounding sphere, maximizes when $\beta = \sqrt{2}$. However, maximizing the dipole moment of the magnet given a sphere size does not ensure a dipole approximation with minimal error; for that, a multipole expansion of the shape is required.

In the following sections, a spherical coordinate system will be used. All primed variables are defined relative to the magnet for integration and all nonprimed coordinates are defined relative to a global coordinate system in which the point of interest \mathbf{p} is defined. In this convention, θ' is measured from the magnetization axis of the material, ϕ' is measured from a convenient axis orthogonal to the magnetization axis (typically along the length of the magnet), and ρ' is defined as a radial distance from the center of the material. In the global frame, \mathbf{p} is the vector from the center of the magnetized material to the point of interest and will be described in a spherical frame with: θ measured from the global z -axis and ϕ pointing in the positive θ direction, ϕ measured from the positive x -axis and ϕ pointing in the positive ϕ direction, and p taken as the magnitude of the \mathbf{p} vector with $\hat{\mathbf{r}}$ pointing in the \mathbf{p} direction (the difference in variable name is to avoid confusion when switching between spherical and coordinate-free descriptions). For reference, Fig. 1 shows the coordinate system with both the global and material coordinate systems aligned.

1) *Axially Magnetized Cylinder*: The multipole expansion defined by (5) is adapted to axially magnetized cylinders by taking $\mathbf{n}' \cdot \mathbf{M}$ to be $M \equiv \|\mathbf{M}\|$ on the top surface, $-M$ on the bottom surface, and 0 on the cylindrical wall

$$\Phi(\mathbf{p}, \beta) = \frac{M}{4\pi} \sum_{n=0}^{\infty} \frac{\left(\frac{L}{2}\right)^{n+2}}{p^{n+1}} D_n(\mathbf{p}, \beta) \quad (12)$$

where

$$D_n(\mathbf{p}, \beta) = \int_0^{2\pi \tan^{-1}(\beta)} \int_0^{\pi} \frac{P_n(\hat{\mathbf{p}} \cdot \hat{\mathbf{p}}') \sin \theta'}{(\cos \theta')^{n+3}} d\theta' d\phi' - (-1)^n \int_0^{2\pi} \int_{\pi - \tan^{-1}(\beta)}^{\pi} \frac{P_n(\hat{\mathbf{p}} \cdot \hat{\mathbf{p}}') \sin \theta'}{(\cos \theta')^{n+3}} d\theta' d\phi'.$$

Using the substitution $x = \cos \theta'$, D_n can be further simplified

$$D_n(\mathbf{p}, \beta) = \begin{cases} 2 \int_0^1 \int_0^{2\pi} \frac{P_n(\hat{\mathbf{p}} \cdot \hat{\mathbf{p}}')}{x^{n+3}} d\phi' dx, & n \text{ odd} \\ 0, & n \text{ even} \end{cases}$$

where

$$\hat{\mathbf{p}} \cdot \hat{\mathbf{p}}' = \sqrt{1 - x^2} \sin \theta (\sin \phi \sin \phi' + \cos \phi \cos \phi') + x \cos \theta. \quad (13)$$

The magnetic field of an axially magnetized cylindrical magnet described in cylindrical coordinates is then

$$\mathbf{B}(\mathbf{p}) = \frac{\mu_0 m}{4\pi V} \sum_{n \text{ odd}} \frac{\left(\frac{L}{2}\right)^{n+2}}{p^{n+2}} \left((n+1) D_n \hat{\mathbf{r}} - \frac{dD_n}{d\theta} \hat{\boldsymbol{\theta}} \right) \quad (14)$$

where m is the magnitude of the dipole moment \mathbf{m} . Noticing that $m \cos \theta \hat{\mathbf{r}} = \hat{\mathbf{p}} \hat{\mathbf{p}}^T \mathbf{m}$ and that $m \sin \theta \hat{\boldsymbol{\theta}} = (\hat{\mathbf{p}} \hat{\mathbf{p}}^T - \mathbf{I}) \mathbf{m}$, the spherical-coordinate field definition can be converted into a coordinate-free form. The first term is the dipole term, as expected. The next two terms will be used in Sections IV-A and IV-C to

find the geometry that maximizes the contribution of the dipole term to total field

$$\begin{aligned} \mathbf{B}_1 &= \frac{\mu_0}{4\pi} \frac{1}{p^3} (3\hat{\mathbf{p}}\hat{\mathbf{p}}^T - \mathbf{I})\mathbf{m} \\ \mathbf{B}_3 &= \frac{\mu_0}{4\pi} \frac{1}{p^5} \left(\frac{L}{2}\right)^2 \left(\frac{4-3\beta^2}{8}\right) \\ &\quad \cdot \left((35(\hat{\mathbf{m}}^T\hat{\mathbf{p}})^2 - 15) \hat{\mathbf{p}}\hat{\mathbf{p}}^T - (15(\hat{\mathbf{m}}^T\hat{\mathbf{p}})^2 - 3) \mathbf{I} \right) \mathbf{m} \\ \mathbf{B}_5 &= \frac{\mu_0}{4\pi} \frac{1}{p^7} \left(\frac{L}{2}\right)^4 \left(\frac{15\beta^4 - 60\beta^2 + 24}{64}\right) \\ &\quad \cdot \left(\left(231(\hat{\mathbf{m}}^T\hat{\mathbf{p}})^4 - \frac{105}{2}(\hat{\mathbf{m}}^T\hat{\mathbf{p}})^2 + 35 \right) \hat{\mathbf{p}}\hat{\mathbf{p}}^T \right. \\ &\quad \left. - (105(\hat{\mathbf{m}}^T\hat{\mathbf{p}})^4 - 70(\hat{\mathbf{m}}^T\hat{\mathbf{p}})^2 + 5) \mathbf{I} \right) \mathbf{m}. \quad (15) \end{aligned}$$

2) *Diametrically Magnetized Cylinder*: Adapting the multipole expansion to diametrically magnetized cylinders requires taking the $\hat{\mathbf{n}}' \cdot \mathbf{M}$ term in (5) to be $M \sin \phi'$ on the cylindrical wall and 0 on the top and bottom surfaces. This aligns the magnetization direction with the Cartesian y -axis, and the scalar potential described by (5) becomes

$$\Phi(\mathbf{p}, \beta) = \frac{M}{4\pi} \sum_{n=0}^{\infty} \frac{\left(\frac{D}{2}\right)^{n+2}}{p^{n+1}} D_n(\mathbf{p}, \beta) \quad (16)$$

where

$$D_n(\mathbf{p}, \beta) = \int_{\tan^{-1}\beta}^{\pi - \tan^{-1}\beta} \int_0^{2\pi} \frac{P_n(\hat{\mathbf{p}} \cdot \hat{\mathbf{p}}') \sin \phi'}{(\sin \theta')^{n+2}} d\phi' d\theta'$$

and

$$\begin{aligned} \hat{\mathbf{p}} \cdot \hat{\mathbf{p}}' &= \cos \theta \sin \theta' \sin \phi' + \cos \phi \sin \theta \cos \theta' \\ &\quad + \sin \phi \sin \theta \sin \theta' \cos \phi'. \end{aligned}$$

The magnetic field described in spherical coordinates is then

$$\begin{aligned} \mathbf{B}(\mathbf{p}) &= \frac{\mu_0}{4\pi} \frac{m}{V} \sum_{n \text{ odd}} \frac{\left(\frac{D}{2}\right)^{n+2}}{p^{n+2}} \left((n+1) D_n \hat{\mathbf{r}} \right. \\ &\quad \left. - \frac{dD_n}{d\theta} \hat{\boldsymbol{\theta}} - \frac{1}{\sin \theta} \frac{dD_n}{d\phi} \hat{\boldsymbol{\phi}} \right). \quad (17) \end{aligned}$$

Noticing that $m \cos \theta \hat{\mathbf{r}} = \hat{\mathbf{p}}\hat{\mathbf{p}}^T \mathbf{m}$, $m \sin \theta \hat{\boldsymbol{\theta}} = (\hat{\mathbf{p}}\hat{\mathbf{p}}^T - \mathbf{I})\mathbf{m}$, and $m \sin \theta \hat{\boldsymbol{\phi}} = -\hat{\mathbf{p}} \times \mathbf{m}$, and defining $\hat{\mathbf{l}}$ to run along the axis of the magnet, the spherical-coordinate field definition can be converted into a coordinate-free form. The first term is the dipole term. The next two terms will be used in Sections IV-A and IV-C

$$\begin{aligned} \mathbf{B}_1 &= \frac{\mu_0}{4\pi} \frac{1}{p^3} (3\hat{\mathbf{p}}\hat{\mathbf{p}}^T - \mathbf{I})\mathbf{m} \\ \mathbf{B}_3 &= \frac{\mu_0}{4\pi} \frac{1}{p^5} \left(\frac{D}{2}\right)^2 \left(\frac{3\beta^2 - 4}{8}\right) \\ &\quad \cdot \left(\left((35(\hat{\mathbf{m}}^T\hat{\mathbf{p}})^2 - 25) \left(\frac{\hat{\mathbf{l}}^T\hat{\mathbf{p}}}{|\hat{\mathbf{p}} \times \hat{\mathbf{m}}|}\right)^2 + 5 \right) \hat{\mathbf{p}}\hat{\mathbf{p}}^T \mathbf{m} \right. \\ &\quad \left. - \left((15(\hat{\mathbf{m}}^T\hat{\mathbf{p}})^2 - 5) \left(\frac{\hat{\mathbf{l}}^T\hat{\mathbf{p}}}{|\hat{\mathbf{p}} \times \hat{\mathbf{m}}|}\right)^2 + 1 \right) \mathbf{m} \right. \\ &\quad \left. + 10 \left(\frac{(\hat{\mathbf{l}}^T\hat{\mathbf{p}})(\hat{\mathbf{m}}^T\hat{\mathbf{p}})(\hat{\mathbf{p}}^T(\hat{\mathbf{m}} \times \hat{\mathbf{l}}))}{|\hat{\mathbf{p}} \times \hat{\mathbf{m}}|^2} \right) \hat{\mathbf{p}} \times \mathbf{m} \right) \end{aligned}$$

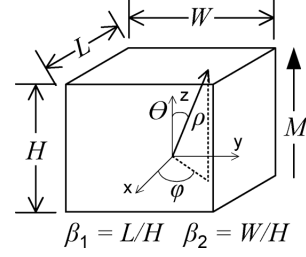


Fig. 2. Definition of a rectangular-cross-section bar magnet geometry.

$$\begin{aligned} \mathbf{B}_5 &= \frac{\mu_0}{4\pi} \frac{1}{p^7} \left(\frac{D}{2}\right)^4 \left(\frac{5\beta^4 - 20\beta^2 + 8}{64}\right) \\ &\quad \cdot \left(21 \left(3(7 - 11(\hat{\mathbf{m}}^T\hat{\mathbf{p}})^2) \frac{(\hat{\mathbf{l}}^T\hat{\mathbf{p}})^4}{|\hat{\mathbf{p}} \times \hat{\mathbf{m}}|^2} \right. \right. \\ &\quad \left. \left. + (18(\hat{\mathbf{m}}^T\hat{\mathbf{p}})^2 - 14) \left(\frac{\hat{\mathbf{l}}^T\hat{\mathbf{p}}}{|\hat{\mathbf{p}} \times \hat{\mathbf{m}}|}\right)^2 + 1 \right) \hat{\mathbf{p}}\hat{\mathbf{p}}^T \mathbf{m} \right. \\ &\quad \left. - 3 \left(21(1 - 5(\hat{\mathbf{m}}^T\hat{\mathbf{p}})^2) \frac{(\hat{\mathbf{l}}^T\hat{\mathbf{p}})^4}{|\hat{\mathbf{p}} \times \hat{\mathbf{m}}|^2} \right. \right. \\ &\quad \left. \left. + (42(\hat{\mathbf{m}}^T\hat{\mathbf{p}})^2 - 14) \left(\frac{\hat{\mathbf{l}}^T\hat{\mathbf{p}}}{|\hat{\mathbf{p}} \times \hat{\mathbf{m}}|}\right)^2 + 1 \right) \mathbf{m} \right. \\ &\quad \left. - 84 \frac{\hat{\mathbf{l}}^T\hat{\mathbf{p}}\hat{\mathbf{m}}^T\hat{\mathbf{p}}\hat{\mathbf{p}}^T(\hat{\mathbf{m}} \times \hat{\mathbf{l}})}{|\hat{\mathbf{p}} \times \hat{\mathbf{m}}|^2} (3(\hat{\mathbf{l}}^T\hat{\mathbf{p}})^2 - 1) \hat{\mathbf{p}} \times \mathbf{m} \right). \quad (18) \end{aligned}$$

B. Rectangular-Cross-Section Bar Magnet

Rectangular bar magnets require two aspect ratios to describe their shape. For this discussion, the height of the magnet H will be taken along the magnetization direction and will be oriented with the z -axis, and β_1 and β_2 will be taken as the length-to-height and width-to-height aspect ratios and will be oriented along the x - and y -axes, respectively. The geometry is shown in Fig. 2. For this geometry, (5) is adapted by taking $\hat{\mathbf{n}}' \cdot \mathbf{M}$ to be $+M$ on the top and $-M$ on the bottom and becomes

$$\Phi(\mathbf{p}) = \frac{M}{4\pi} \sum_{n=0}^{\infty} \frac{D_n(\mathbf{p}, \beta_1, \beta_2)}{p^{n+1}} \quad (19)$$

where

$$\begin{aligned} D_n(\mathbf{p}, \beta_1, \beta_2) &= \int_{-\beta_2 H/2}^{\beta_2 H/2} \int_{-\beta_1 H/2}^{\beta_1 H/2} (\rho')^n P_n(\hat{\mathbf{p}} \cdot \hat{\mathbf{p}}') dx' dy' \Big|_{z'=H/2} \\ &\quad - \int_{-\beta_2 H/2}^{\beta_2 H/2} \int_{-\beta_1 H/2}^{\beta_1 H/2} (\rho')^n P_n(\hat{\mathbf{p}} \cdot \hat{\mathbf{p}}') dx' dy' \Big|_{z'=-H/2} \end{aligned}$$

and

$$\hat{\mathbf{p}} \cdot \hat{\mathbf{p}}' = \frac{x' \cos \phi \sin \theta + y' \sin \phi \sin \theta + z' \cos \theta}{\sqrt{x'^2 + y'^2 + z'^2}}.$$

D_n can be further simplified to

$$D_n(\mathbf{p}, \beta_1, \beta_2) = \begin{cases} 2 \int_{-\beta_2 H/2}^{\beta_2 H/2} \int_{-\beta_1 H/2}^{\beta_1 H/2} (\rho')^n P_n(\hat{\mathbf{p}} \cdot \hat{\rho}') dx' dy' \Big|_{z=\frac{H}{2}}, & n \text{ odd} \\ 0, & n \text{ even.} \end{cases}$$

The magnetic field described in spherical coordinates is then

$$\mathbf{B}(\mathbf{p}) = \frac{\mu_0}{4\pi} \frac{m}{V} \sum_{n \text{ odd}} \frac{1}{p^{n+2}} \left((n+1) D_n \hat{\mathbf{r}} - \frac{dD_n}{d\theta} \hat{\boldsymbol{\theta}} - \frac{1}{\sin \theta} \frac{dD_n}{d\phi} \hat{\boldsymbol{\phi}} \right). \quad (20)$$

Defining $\hat{\mathbf{l}}$ to point along the L direction, and noticing that $m \cos \theta \hat{\mathbf{r}} = \hat{\mathbf{p}} \hat{\mathbf{p}}^T \mathbf{m}$, $m \sin \theta \hat{\boldsymbol{\theta}} = (\hat{\mathbf{p}} \hat{\mathbf{p}}^T - \mathbf{I}) \mathbf{m}$, $m \sin \theta \hat{\boldsymbol{\phi}} = -\hat{\mathbf{p}} \times \mathbf{m}$, $\cos \phi = \hat{\mathbf{p}}^T \hat{\mathbf{l}} / |\hat{\mathbf{p}} \times \hat{\mathbf{m}}|$, and $\sin \phi = \hat{\mathbf{p}}^T (\hat{\mathbf{m}} \times \hat{\mathbf{l}}) / |\hat{\mathbf{p}} \times \hat{\mathbf{m}}|$, the spherical-coordinate field definition can be converted into a coordinate-free form. The first term is the dipole term. The next term will be used in Section IV-B

$$\begin{aligned} \mathbf{B}_1 &= \frac{\mu_0}{4\pi} \frac{1}{p^3} (3\hat{\mathbf{p}} \hat{\mathbf{p}}^T - \mathbf{I}) \mathbf{m} \\ \mathbf{B}_3 &= \frac{\mu_0}{4\pi} \frac{H^2}{8p^5} \left(5 \left((\beta_1^2 - \beta_2^2) (\hat{\mathbf{m}}^T \hat{\mathbf{p}})^2 + 5 \right) \left(\frac{\hat{\mathbf{p}}^T \hat{\mathbf{l}}}{|\hat{\mathbf{p}} \times \hat{\mathbf{m}}|} \right)^2 \right. \\ &\quad \left. - 7(\beta_1^2 - 1)(\hat{\mathbf{m}}^T \hat{\mathbf{p}})^2 - \beta_1^2 + 4\beta_2^2 - 3 \right) \hat{\mathbf{p}} \hat{\mathbf{p}}^T \mathbf{m} \\ &\quad + \left(5(\beta_1^2 - \beta_2^2) \left(\frac{\hat{\mathbf{p}}^T \hat{\mathbf{l}}}{|\hat{\mathbf{p}} \times \hat{\mathbf{m}}|} \right)^2 (3(\hat{\mathbf{m}}^T \hat{\mathbf{p}})^2 \mathbf{l}) \right. \\ &\quad \left. + 15(\beta_2^2 - 1)(\hat{\mathbf{m}}^T \hat{\mathbf{p}})^2 + \beta_1^2 - 4\beta_2^2 + 3 \right) \mathbf{m} \\ &\quad + \frac{5(\beta_2^2 - \beta_1^2)}{2} \frac{(\hat{\mathbf{p}}^T \hat{\mathbf{l}})(\hat{\mathbf{p}}^T (\hat{\mathbf{m}} \times \hat{\mathbf{l}}))}{|\hat{\mathbf{p}} \times \hat{\mathbf{m}}|^2} \\ &\quad \times (\hat{\mathbf{m}}^T \hat{\mathbf{p}}) \hat{\mathbf{p}} \times \mathbf{m} \Big). \end{aligned} \quad (21)$$

C. Validation of Multipole Expansions With FEA Solutions

To verify the validity of the expansions, the first nine nonzero terms of the multipole expansions are compared to FEA simulations solved by Ansoft Maxwell version 14.0. A cross-sectional contour plot showing the relative error between the multipole expansion and the FEA simulation for axially and diametrically magnetized cylinders and rectangular-cross-section bars are shown in Fig. 3. The average and maximum errors at a given distance are shown in Fig. 4. These comparisons demonstrate that the first nine terms of the multipole model are quite accurate for distances greater than 1.5 minimum-bounding-sphere radii.

IV. OPTIMAL GEOMETRIC RELATIONS FOR DIPOLE APPROXIMATION

A. Cylinders

In both the axially magnetized and diametrically magnetized conditions, the cylindrical magnet has the same shape-dependent factors in the multipole expansion, as shown by the second

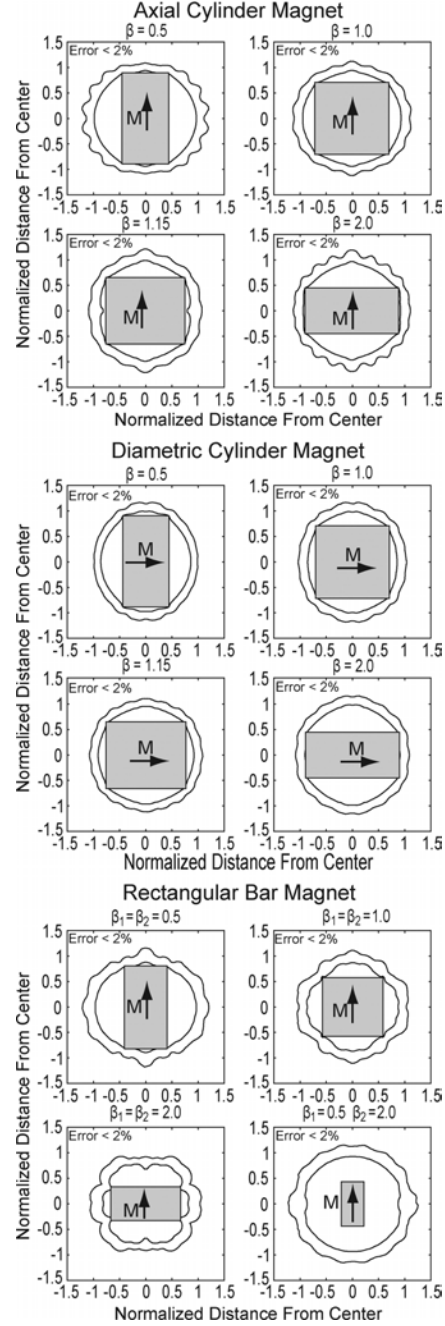


Fig. 3. Contour plot showing the 2% (outer) and 50% (inner) bands of error between the multipole expansion and the FEA model for several geometries of cylinder and rectangular magnets. Note that the error drops to below 2% after 1.5 radii of the minimum bounding sphere for each.

terms in (15) and (18), respectively. Using the far-field criterion for an optimal approximation geometry, the optimal β is defined by the equation $4 - 3\beta^2 = 0$. Therefore, the far-field optimal

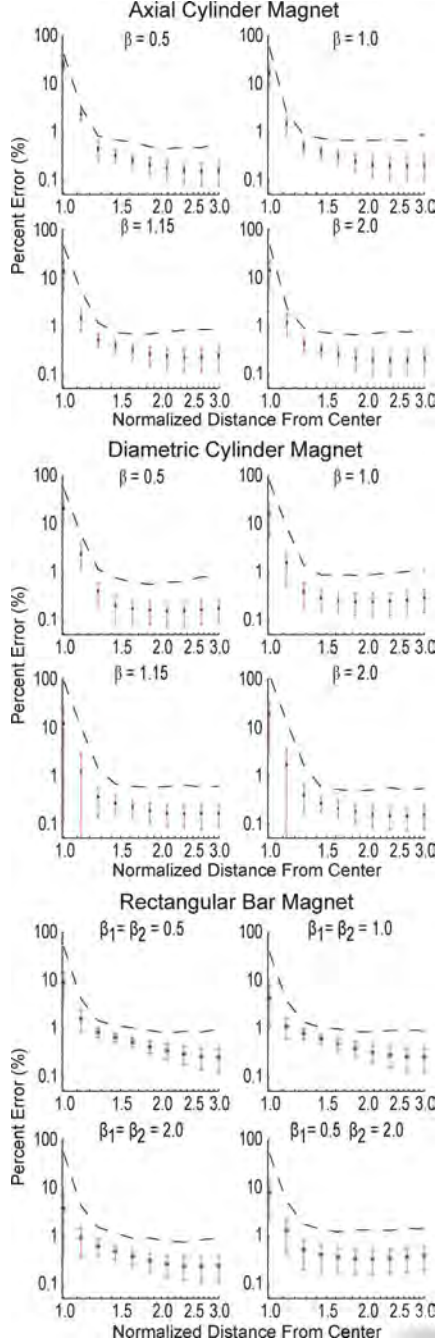


Fig. 4. The average error of the first nine terms of the multipole approximation as compared to FEA simulation over a spherical surface as a function of distance for several different geometries of cylinder and rectangular magnets. The dashed line represents the maximum error and the error bands ± 1 standard deviation about the average error.

β for both the diametrically magnetized and axially magnetized conditions is $\beta = \sqrt{4/3} \approx 1.15$. This aspect ratio corresponds

to a 3% compromise in magnet volume and, therefore, dipole moment from the maximum given a minimum bounding sphere, which occurs when $\beta = \sqrt{2}$.

B. Rectangular-Cross-Section Bar

The optimal dipole approximation for a rectangular-cross-section bar can be obtained by determining which values of β_1 and β_2 set the \mathbf{B}_3 term in the multipole expansion defined in (21) to zero. Inspection of (21) shows that $\beta_1 = \beta_2 = 1$ is the only solution that sets every component of the \mathbf{B}_3 coefficient to zero. Conveniently, this cubic geometry also corresponds to the maximum dipole moment for a given minimum bounding sphere.

C. Axially Magnetized Washer

As superposition holds for permanent magnet materials with low recoil susceptibilities (i.e., an externally applied or self-generated field does not appreciably affect the magnetization of the material), the optimal dipole shape for the washer shown in Fig. 5 can be defined by a linear combination of two cylinders of equal length. The larger diameter cylinder is taken to have a magnetization of \mathbf{M} and a diameter-to-length ratio of β_1 and the smaller is taken to have a magnetization of $-\mathbf{M}$ and a diameter-to-length ratio of β_2 . The volumes that these two cylinders overlap is equivalent to a hole in the larger cylinder. Following the procedure outlined previously, the equation that defines the optimal dipole approximation geometry for an axially magnetized washer is a linear combination of the \mathbf{B}_3 coefficients from (15) of the two cylinders scaled by their volumes (V_1 and V_2)

$$V_1 \left(\frac{L}{2} \right)^2 \frac{4 - 3\beta_1^2}{8} - V_2 \left(\frac{L}{2} \right)^2 \frac{4 - 3\beta_2^2}{8} = 0. \quad (22)$$

There is a real solution when $\sqrt{2/3} < \beta_1 \leq \sqrt{4/3}$

$$\beta_2 = \frac{\sqrt{12 - 9\beta_1^2}}{3}. \quad (23)$$

Outside this range, the optimal dipole approximation is defined by minimizing the square of the quadrupole coefficient and is equivalent to having no hole or no magnet. Moreover, the only real values of β_1 and β_2 subject to (23) that minimize the hexapole \mathbf{B}_5 coefficient are $\sqrt{4/3}$ and 0, respectively. That is, adding a hole to a nonoptimal configuration can make the approximation better, but the best geometry for dipole approximation has no hole. If a hole is desired, the optimal washer length can be calculated by substituting the definitions of β_1 and β_2 into (23) and solving for L , and is

$$L = \sqrt{\frac{3}{4} (D_1^2 + D_2^2)}. \quad (24)$$

D. Diametrically Magnetized Washer

For a diametrically magnetized washer, the optimal hole size is defined by a linear combination of the \mathbf{B}_3 coefficients from (18) of the two cylinders scaled by their volume

$$V_1 \left(\frac{D_1}{2} \right)^2 \frac{3\beta_1^2 - 4}{8} - V_2 \left(\frac{D_2}{2} \right)^2 \frac{3\beta_2^2 - 4}{8} = 0 \quad (25)$$

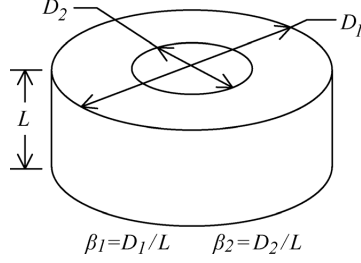


Fig. 5. Definition of washer-shaped magnet geometry.

which exists when $(2\sqrt{2}/3) < \beta_1 < \sqrt{4/3}$ and is equal to

$$\beta_2 = \sqrt{\frac{1}{6} \left(\sqrt{(4 - 3\beta_1^2)(9\beta_1^2 + 4)} + 4 - 3\beta_1^2 \right)}. \quad (26)$$

Using this equation to define the relationship between β_1 and β_2 , the magnitude of the hexapole term in (18) can be minimized

$$\left| V_1 \left(\frac{D_1}{2} \right)^4 \frac{5\beta_1^4 - 20\beta_1^2 + 8}{64} - V_2 \left(\frac{D_2}{2} \right)^4 \frac{5\beta_2^4 - 20\beta_2^2 + 8}{64} \right| \rightarrow 0 \quad (27)$$

which minimizes when $\beta_1 = \beta_2 = 2\sqrt{2}/3$ or, equivalently, the no-magnet geometry (i.e., the hole is the same size as the magnet). If (27) is normalized by the remaining dipole moment ($\|\mathbf{M}\|(V_1 - V_2)$), the resulting formula minimizes at the no-hole geometry; that is, the optimal geometry for a diametrically magnetized cylindrical magnet has no hole. If a hole is desired for a diametrically magnetized magnet, the optimal length is

$$L = \sqrt{\frac{3}{4} \left(\frac{D_1^4 + D_1^2 D_2^2 + D_2^4}{D_1^2 + D_2^2} \right)}. \quad (28)$$

V. ERROR CHARACTERIZATION OF OPTIMAL DIPOLE GEOMETRIES

The average percent error over the surface of a sphere associated with the dipole approximation can be quantified by averaging (10) over the surface of a sphere (and multiplying by 100). The average error as a function of distance from the center of the magnet is given for axially magnetized cylinders, diametrically magnetized cylinders, and rectangular-cross-section rods in Fig. 6.

The crossover between the $\beta = 1$ and $\beta = \sqrt{4/3}$ error curves, shown in the diametrically magnetized cylindrical magnet error plot, indicate that a geometry other than the far-field optimal will minimize the dipole approximation error for distances close to the surface of the magnet. Numerical analysis of diametrically magnetized cylinder magnets indicates that $\beta = 1.10$ minimizes the dipole approximation error for distances between 1 and 4 minimum-bounding-sphere radii; however, the optimal near-field geometry provides only a marginal reduction in error when compared to the far-field optimal geometry at those distances.

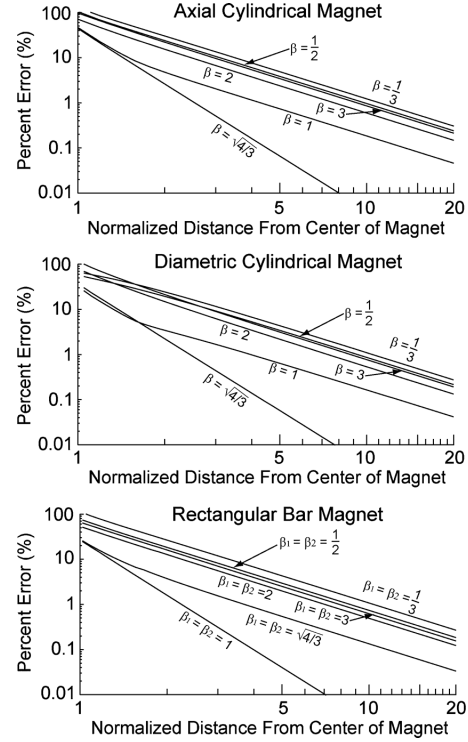


Fig. 6. The average errors associated with different geometries of cylindrical and rectangular permanent magnets are plotted as a function of distance from the center of the magnet. Distances are normalized by the radius of the minimum bounding sphere.

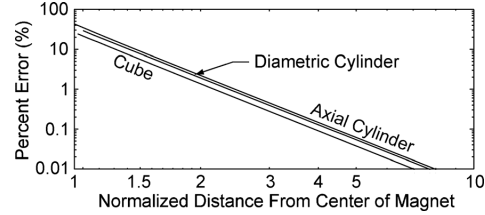


Fig. 7. The error associated with the optimal dipole geometries. The cube-shaped magnet has the least dipole approximation error, followed by the diametrically magnetized cylinder.

A comparison of the average error associated with the optimal geometries for the cylindrical and rectangular-cross-section bar magnets is shown in Fig. 7. The average error associated with the different optimal geometries is very close, with the cubic magnet having the least and the axially magnetized magnet having the most. Figs. 8 and 9 show the variation of error as a function of angle at a given distance. To determine the error at a given position, it is only necessary to multiply the average error given in Fig. 7 by the value in the error variation plot that corresponds to the angular position.

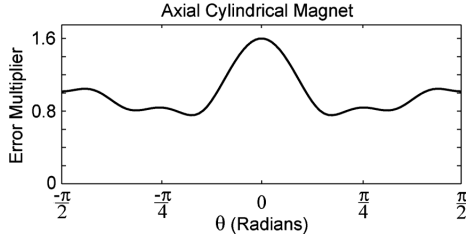


Fig. 8. Variation in dipole approximation error as a function of angle for an axially magnetized cylindrical magnet with $\beta = \sqrt{4/3}$. The magnetization axis of the magnet corresponds to $\theta = 0$. See Fig. 1.

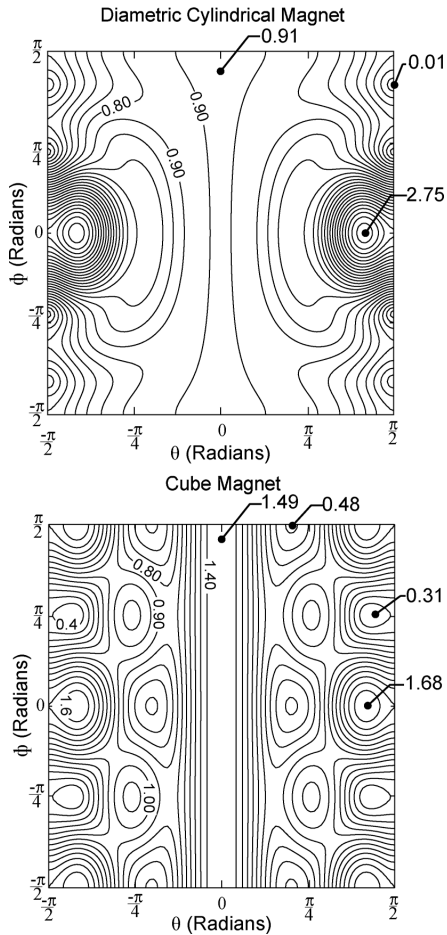


Fig. 9. Variation in dipole approximation error as a function of angle for an optimal diametrically magnetized cylindrical magnet and cube magnet. Each contour line represents a step in 0.1 times the average error at a given radius. The magnetization axis corresponds to $\theta = 0$ and the \hat{l} direction corresponds to $\theta = \pi/2$ and $\phi = 0$. See Figs. 1 and 2.

The diametrically magnetized cylinder has both the highest average error and the largest error range, which appears in conflict with the observations in the work by Fountain *et al.* [21],

which shows diametrically magnetized magnets are preferable to the axially magnetized magnets. However, upon closer inspection, the least squares fit of the dipole approximation in the work by Fountain *et al.* is based on field measurements taken only along the magnetization axis of the magnet. At those locations, Figs. 7–9 predict a lower error for diametrically magnetized magnets than axially magnetized magnets, since the average error is approximately the same and the error multiplier for $\theta = 0$ is 0.91 versus 1.6, respectively. Because Fountain *et al.* took their data along the magnetization axis, the dipole fit not only was better for the diametrically magnetized magnets, but also was more accurate in determining the dipole moment of the magnet. This also explains why Fountain *et al.* calculated different dipole moments based on their measured data for the axially magnetized magnet and the diametrically magnetized magnet despite both magnets having the same volume and material.

VI. CONCLUSION

The multipole expansion provides an accurate method for determining the field generated by a permanent magnet for positions away from the surface of the magnet. This expansion also provides a direct way to determine the optimal dipole approximation geometric parameters for various shapes of magnets. This optimal geometry for cylinders (both axially and diametrically magnetized) is a diameter-to-length ratio of $\sqrt{4/3}$ and, for rectangular-cross-section bars, it is a cube. By choosing these ratios, the error associated with the dipole model is reduced compared to nonoptimal geometries, as shown by the trend depicted in Fig. 6. The accuracy of the approximation increases faster with distance for optimal geometries than it does for nonoptimal geometries. Given a minimum bounding sphere, there is no reduction in dipole moment magnitude from the maximum in rectangular bars to achieve an optimal dipole approximation and the reduction required in cylinders is less than 3%. Of the geometries studied for a given distance from the magnet, the cubic magnet has the least average dipole approximation error followed closely by the diametric and axial magnets. The axially magnetized cylindrical magnet has the smallest range in error at a given distance from the center of the magnet.

ACKNOWLEDGMENT

This work was supported by the National Science Foundation under Grants 0952718 and 0654414.

REFERENCES

- [1] M. Hämäläinen, R. Hari, R. J. Ilmoniemi, J. Knuutila, and O. V. Lounasmaa, "Magnetoencephalography—Theory, instrumentation, and applications to noninvasive studies of the working human brain," *Rev. Mod. Phys.*, vol. 65, pp. 413–497, 1993.
- [2] F. Raab, E. Blood, T. Steiner, and H. Jones, "Magnetic position and orientation tracking system," *IEEE Trans. Aerosp. Electron. Syst.*, vol. AES-15, no. 5, pp. 709–718, Sep. 1979.
- [3] A. Sheinker, L. Frumkis, B. Ginzburg, N. Salomonski, and B.-Z. Kaplan, "Magnetic anomaly detection using a three-axis magnetometer," *IEEE Trans. Magn.*, vol. 45, no. 1, pp. 160–167, Jan. 2009.
- [4] M. Birsan, "Recursive Bayesian method for magnetic dipole tracking with a tensor gradiometer," *IEEE Trans. Magn.*, vol. 47, no. 2, pp. 409–415, Feb. 2011.

- [5] E. Paperno, I. Sasada, and E. Leonovich, "A new method for magnetic position and orientation tracking," *IEEE Trans. Magn.*, vol. 37, no. 4, pp. 1938–1940, Jul. 2001.
- [6] C. Hu, M. Q. Meng, and M. Mandal, "Efficient magnetic localization and orientation technique for capsule endoscopy," in *Proc. IEEE/RSJ Int. Conf. Intell. Robots Syst.*, 2005, pp. 628–633.
- [7] C. Hu, M. Q. Meng, and M. Mandal, "The calibration of 3-axis magnetic sensor array system for tracking wireless capsule endoscope," in *Proc. IEEE/RSJ Int. Conf. Intell. Robots Syst.*, Oct. 2006, pp. 162–167.
- [8] C. Hu, M. Q. Meng, and M. Mandal, "A linear algorithm for tracing magnet position and orientation by using three-axis magnetic sensors," *IEEE Trans. Magn.*, vol. 43, no. 12, pp. 4096–4101, Dec. 2007.
- [9] C. Hu, M. Li, S. Song, W. Yang, R. Zhang, and M.-H. Meng, "A cubic 3-axis magnetic sensor array for wirelessly tracking magnet position and orientation," *IEEE Sensors*, vol. 10, no. 5, pp. 903–913, May 2010.
- [10] C. Hu, S. Song, X. Wang, M. Meng, and B. Li, "A novel positioning and orientation system based on 3-axis magnetic coils," *IEEE Trans. Magn.*, 2012, to be published.
- [11] X. Wang and M. Meng, "Dipole modeling of magnetic marker for capsule endoscope localization," in *Proc. World Congr. Intell. Control Autom.*, 2006, vol. 2, pp. 5382–5386.
- [12] X. Wang and M. Q.-H. Meng, "Application of a magnetic dipole modelling approach to the problem of tracking a capsule endoscope," *Proc. Inst. Mech. Eng. H/J. Eng. Med.*, vol. 225, no. 4, pp. 377–398, Apr. 2011.
- [13] J. Baldoni and B. Yellen, "Magnetic tracking system: Monitoring heart valve prostheses," *IEEE Trans. Magn.*, vol. 43, no. 6, pp. 2430–2432, Jun. 2007.
- [14] S. Song, C. Hu, M. Li, W. Yang, and M.-H. Meng, "Two-magnet-based 6d-localization and orientation for wireless capsule endoscope," in *Proc. IEEE Int. Conf. Robot. Biomimetics*, Dec. 2009, pp. 2338–2343.
- [15] G. Ciuti, P. Valdastrì, A. Menciassi, and P. Dario, "Robotic magnetic steering and locomotion of capsule endoscope for diagnostic and surgical endoluminal procedures," *Robotica*, vol. 28, no. Special Issue 02, pp. 199–207, 2010.
- [16] W. Yang, C. Hu, M. Li, M.-H. Meng, and S. Song, "A new tracking system for three magnetic objectives," *IEEE Trans. Magn.*, vol. 46, no. 12, pp. 4023–4029, Dec. 2010.
- [17] M. Li, S. Song, C. Hu, D. Chen, and M.-H. Meng, "A novel method of 6-DOF electromagnetic navigation system for surgical robot," in *Proc. World Congr. Intell. Control Autom.*, Jul. 2010, pp. 2163–2167.
- [18] T. Nara, H. Watanabe, and W. Ito, "Divergence form of Euler's equation for magnetic dipole localization," in *Proc. SICE Annu. Conf.*, Sep. 2011, pp. 2356–2360.
- [19] W. Fang and H. Son, "Optimization of measuring magnetic fields for position and orientation tracking," *IEEE/ASME Trans. Mechatron.*, vol. 16, no. 3, pp. 440–448, Jun. 2011.
- [20] M. Salerno, G. Ciuti, G. Lucarini, R. Rizzo, P. Valdastrì, A. Menciassi, A. Landi, and P. Dario, "A discrete-time localization method for capsule endoscopy based on on-board magnetic sensing," *Meas. Sci. Technol.*, vol. 23, no. 1, 2012, 015701.
- [21] T. W. R. Fountain, P. V. Kailat, and J. J. Abbott, "Wireless control of magnetic helical microrobots using a rotating-permanent-magnet manipulator," in *Proc. IEEE Int. Conf. Robot. Autom.*, 2010, pp. 576–581.
- [22] B. J. Nelson, I. K. Kaliakatos, and J. J. Abbott, "Microrobots for minimally invasive medicine," *Annu. Rev. Biomed. Eng.*, vol. 12, no. 1, pp. 55–85, 2010.
- [23] A. W. Mahoney and J. J. Abbott, "Managing magnetic force applied to a magnetic device by a rotating dipole field," *Appl. Phys. Lett.*, vol. 99, 2011, 134103.
- [24] A. W. Mahoney, D. L. Cowan, K. M. Miller, and J. J. Abbott, "Control of untethered magnetically actuated tools using a rotating permanent magnet in any position," in *Proc. IEEE Int. Conf. Robot. Autom.*, 2012, pp. 3375–3380.
- [25] M. Beleggia, M. D. Graef, Y. T. Millev, D. A. Goode, and G. Rowlands, "Demagnetization factors for elliptic cylinders," *J. Phys. D, Appl. Phys.*, vol. 38, pp. 3333–3342, 2005.
- [26] J. A. Osborn, "Demagnetizing factors of the general ellipsoid," *Phys. Rev.*, vol. 67, pp. 351–357, Jun. 1945.
- [27] P. Rhodes and G. Rowlands, "Demagnetising energies of uniformly magnetised rectangular blocks," *Proc. Leeds Phil. Liter. Soc.*, vol. 6, pp. 191–210, 1954.
- [28] A. Aharoni, "Demagnetizing factors for rectangular ferromagnetic prisms," *J. Appl. Phys.*, vol. 86, pp. 3432–3434, 1998.
- [29] J. D. Jackson, *Classical Electrodynamics*. New York: Wiley, 1975.
- [30] D. J. Griffiths, *Introduction to Electrodynamics*. Englewood Cliffs, NJ: Prentice-Hall, 1999.

CHAPTER 3

OMNIMAGNET: AN OMNIDIRECTIONAL ELECTROMAGNET FOR CONTROLLED DIPOLE- FIELD GENERATION

Using the tools developed in the last chapter, namely using a multipole expansion to characterize the field associated with a magnetic source and then minimizing the quadruple term to obtain an optimized dipole-field source, an electromagnet capable of being modeled by the dipole-field is developed. This design is then optimized for strength by selecting the appropriate core diameter such that the system's dipole-moment per applied-current is maximized. This paper has been accepted for publication in IEEE Transactions on Magnetics and is reprinted here with permission.

A. J. Petruska and J. J. Abbott, "Omnimagnet: An omnidirectional electromagnet for controlled dipole-field generation," *IEEE Trans Magn*, vol. 50, no. 7, pp. 1–10, 2014

©2014 IEEE. Personal use of this material is permitted. Permission from IEEE must be obtained for all other uses, in any current or future media, including reprinting/republishing this material for advertising or promotional purposes, creating new collective works, for resale or redistribution to servers or lists, or reuse of any copyrighted component of this work in other works.

Omnimagnet: An Omnidirectional Electromagnet for Controlled Dipole-Field Generation

Andrew J. Petruska and Jake J. Abbott

Department of Mechanical Engineering, University of Utah, Salt Lake City, UT 84112 USA

An Omnimagnet is an omnidirectional electromagnet comprising a spherical ferromagnetic core inside of three orthogonal nested solenoids. It generates a magnetic dipole field with both a variable dipole-moment magnitude and orientation with no moving parts. The magnetic and physical properties (e.g., dipole moment, weight, resistance, and inductance) of any Omnimagnet are derived. These general relationships are used to design an optimal Omnimagnet subject to the constraints that it has the same dipole-moment per applied current in any direction, each solenoid has no quadrupole contribution to the magnetic field, and the spherical core size maximizes the strength of the resulting dipole field. This optimal design is analyzed using FEA tools and is verified to be dipole-like in nature. Finally, the optimal design is constructed and its utility is demonstrated by driving a helical capsule-endoscope mockup through a transparent lumen.

Index Terms—Magnetic Manipulation, Magnetic dipoles, Electromagnets, Spherical Core

I. INTRODUCTION

MAGNETIC microscale and mesoscale devices (both tethered and untethered) can be manipulated with an externally generated magnetic field, which applies a combination of force and torque to the device without any mechanical connection. Although a combination of permanent magnets and electromagnets can be used to produce the magnetic field required for a manipulation task, some tasks seem better suited to either permanent-magnet or electromagnet systems. Because they have more direct real-time control of the applied magnetic field, electromagnet systems have been used for multi-degree-of-freedom levitation and position/orientation control [1]–[8]. Permanent magnets, which require no electrical power to generate a strong field, have been used for pulling and rolling tasks in which the environment provides some structure [9]–[12], as well as for quasistatic pointing tasks of tethered devices such as magnetic catheters [13]. Because both attractive and lateral forces can be generated between a rotating dipole source and a sympathetically rotating magnetic device, a rotating dipole field could be more effective for rolling/screwing propulsion than the rotating uniform field generated by many electromagnet systems [14]. Finally, it is challenging to scale many laboratory electromagnetic systems that surround their workspace (e.g., Helmholtz coils) to a size that would be required for medical applications, whereas manipulation systems that utilize dipole fields can be located adjacent to their workspace.

An omnidirectional electromagnet, formed by any set of collocated electromagnets that have dipole moments spanning \mathbb{R}^3 , combines the real-time control of field strength associated with traditional electromagnets and the control of dipole orientation associated with rotating permanent magnets. In this paper we describe the Omnimagnet, a subclass of omnidirectional electromagnets that comprise a ferromagnetic core surrounded by three orthogonal solenoids. Specifically, we optimize an

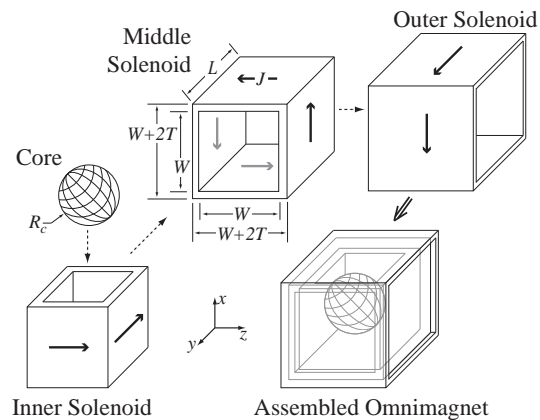


Fig. 1. The assembled Omnimagnet forms a cube constructed of three nested orthogonal solenoids surrounding a spherical core of ferromagnetic material. Each square-cross-section solenoid has a different inner width W , winding thickness T , length L , and associated current density J .

Omnimagnet comprising a spherical core and square-cross-section solenoids (Fig. 1), but other design variations could be considered. An Omnimagnet creates a fully controllable dipole-like magnetic field, contains no moving parts, and becomes inert when powered down—reducing the safety concerns associated with permanent-magnet field sources. The concept of three nested solenoids has been explored as a method of magnetic localization [15] and inductive power coupling [16], but never with a spherical core, and never as a dipole-like magnetic manipulator.

The paper is structured as follows. First, the general design problem for an Omnimagnet is presented. Next, the magnetic fields generated by the three solenoids are described using a multipole expansion of the magnetostatic equations, and the contribution of the ferromagnetic core is quantified.

Corresponding author: A. J. Petruska (e-mail: Andrew.Petruska@utah.edu)

The optimization of a specific Omnimagnet follows, and the design is described. The field generated by this design is then compared to a dipole-field approximation. The inverse solution for determining the dipole moment, and thus the currents, required to produce a desired static or rotating field at a given location is provided. Finally, the capability of the Omnimagnet for the control of untethered magnetic devices is then demonstrated by driving a mockup capsule endoscope through a lumen. This paper expands on our result originally presented in [17] by providing: a more detailed treatment of the quadruple minimization, methods for calculating other relevant mechanical, electrical, and magnetic properties, and an analysis of how extraneous magnetic fields will affect the core magnetization.

II. DESIGN AND OPTIMIZATION

The general concept of an Omnimagnet is broad, consisting of three orthogonal nested solenoids surrounding a ferromagnetic core; however, design choices must be made to realize and optimize a physical Omnimagnet. First, we chose the shape of the solenoids to be square-cross-sectional sleeves to result in a dense packing (see Fig. 1). Next, we chose the core to be a sphere because a spherical core has three desirable properties [18]:

- A sphere does not have a preferential magnetization direction.
- When placed in a uniform field (similar to the field in the center of a solenoid), a sphere produces a pure dipole field.
- The average applied magnetic field within a sphere is equal to the applied magnetic field at the center of the sphere.

We chose that the dipole moment generated in each direction, which consists of the contribution of both an individual solenoid and the magnetization of the core due to that solenoid, should be the same when an equal electrical current density is applied through each solenoid. Other geometric design choices (e.g., cylindrical solenoids or a cubic core) or dipole-moment relationships (e.g., scaling the dipole moment of each solenoid with its heat-transfer capability), could also be pursued using the general framework for Omnimagnet design outlined below. Finally, we constrain our design to use a single wire gauge for all solenoids, which means that “an equal electrical current density” is synonymous with “an equal current”; current and current density are related by the cross-sectional area of the wire used. Throughout this paper, I will be used to refer to currents in units $\{A\}$ and J will be used to refer to current density in units $\{A \cdot m^{-2}\}$. Because current density is invariant to wire selection, the optimization for shape is performed using J ; general discussion, however, will use I , as it is the more natural parameter from a control perspective. The final design of the Omnimagnet shown in Fig. 1 requires ten total constraints (the length, width, and thickness of each solenoid, and the radius of the core).

The magnetic field generated by the Omnimagnet can be represented by the field contributed by the magnetized spherical core superimposed with the field contributed by the

solenoids. Modeling the total field can be performed using FEA tools with a resolution limited by the number of elements used. Alternatively, an analytical dipole approximation can be used to model the field. The dipole approximation provides a closed-form vector equation that can be used to calculate the field generated at a point, or inverted to determine the current necessary to create a particular field. The closer the Omnimagnet is to generating a pure dipole field, the better the algorithms based on this approximation will perform (e.g., [12], [14], [15], [19], [20]). By correctly choosing the solenoids' aspect ratios, the dipole-approximation error can be minimized as a part of the design optimization.

A. Solenoid Multipole Field Expansion

For positions outside of the Omnimagnet's minimum-bounding sphere (i.e., the smallest sphere that the Omnimagnet can fit within), the solenoids' fields can be represented by a multipole expansion of a vector potential [18]:

$$\mathbf{B}(\mathbf{p}) = \nabla \times \Psi(\mathbf{p}) \quad (1)$$

$$\Psi(\mathbf{p}) = \frac{\mu_0}{4\pi} \sum_{n=0}^{\infty} \frac{1}{\|\mathbf{p}\|^{n+1}} \int_{V_s} \mathbf{J}(\mathbf{r}) \|\mathbf{r}\|^n P_n(\hat{\mathbf{p}} \cdot \hat{\mathbf{r}}) dV \quad (2)$$

where $\mu_0 = 4\pi \times 10^{-7} \text{ T} \cdot \text{m} \cdot \text{A}^{-1}$ is the magnetic permeability of free space, \mathbf{p} is the vector (with associated unit vector $\hat{\mathbf{p}}$) from the center of the Omnimagnet to the point of interest in units $\{m\}$, \mathbf{r} is the vector (with associated unit vector $\hat{\mathbf{r}}$) from the center of the Omnimagnet to the point in the solenoid being integrated, $\mathbf{J}(\mathbf{r})$ is the current density vector that points in the direction of the current flow at location \mathbf{r} , V_s represents the solenoid's volume, and $P_n(\cdot)$ are the Legendre polynomials. Since the divergence of a magnetic field through a closed surface must be zero, all of the even terms (those corresponding to P_0, P_2, \dots) must be zero, leaving only the odd terms. The first non-zero term in the multipole expansion (corresponding to P_1) is the dipole field, which can be expressed in a coordinate-free form:

$$\mathbf{B}(\mathbf{p}) = \frac{\mu_0}{4\pi \|\mathbf{p}\|^3} (3\hat{\mathbf{p}}\hat{\mathbf{p}}^T - \mathbb{I}) \mathbf{m} \quad (3)$$

where \mathbb{I} is a 3×3 identity matrix and \mathbf{m} is the dipole moment in units $\{A \cdot m^2\}$. The dipole moment for a current density of any configuration is [18]:

$$\mathbf{m} = \frac{1}{2} \int_{V_s} \mathbf{r} \times \mathbf{J}(\mathbf{r}) dV \quad (4)$$

The dipole moment for a square-cross-section solenoid as shown in Fig. 1 with uniform current density (i.e., the current density does not vary along the thickness or length of the solenoid) is:

$$\mathbf{m} = \frac{JL^4}{6} (\beta_2^3 - \beta_1^3) \hat{\mathbf{l}} \quad (5)$$

where $J = \|\mathbf{J}\|$, L is the axial length of the solenoid (with associated axial unit vector $\hat{\mathbf{l}}$), and $\beta_1 = w/L$ and $\beta_2 = (w+2t)/L$ respectively describe the inner-width-to-length and outer-width-to-length aspect ratios.

The maximum dipole moment that any electromagnet with a bounding cube of edge length L containing no ferromagnetic

material could generate in one direction can be calculated by (5) with $\beta_1 = 0$ and $\beta_2 = 1$, and is $JL^4/6$. The maximum theoretical dipole moment that could be expected for any cubic *omnidirectional* electromagnet with edge length L containing no ferromagnetic material is thus $1/3$ of the unidirectional case: $JL^4/18$; this quantity is used throughout the paper to normalize the strength for a nondimensional optimization, although constructing such an idealized omnidirectional electromagnet would be very challenging.

We show in [21] that by varying the aspect ratios of a rectangular permanent magnet, the dipole-field approximation error can be minimized. The approach finds the geometry that sets the next term in the multipole expansion, the quadrupole term, to zero in the scalar potential of the magnetic field. Using the same technique, but using the vector potential instead of a scalar potential, the magnetic field of each solenoid can be shaped to produce a dipole-like field by removing the quadrupole contribution to the multipole expansion. The quadrupole term for a square-cross-section solenoid of uniform current density corresponds to the P_3 term in the expansion:

$$\mathbf{B}_{\text{quad}}(\mathbf{p}) = \frac{\mu_0}{4\pi} \frac{1}{\|\mathbf{p}\|^5} \left((35(\hat{\mathbf{m}}^T \hat{\mathbf{p}})^2 - 15) \hat{\mathbf{p}} \hat{\mathbf{p}}^T - (15(\hat{\mathbf{m}}^T \hat{\mathbf{p}})^2 - 3) \mathbb{I} \right) \mathbf{m}_{\text{quad}} \quad (6)$$

where \mathbf{m}_{quad} is the quadrupole moment, given by:

$$\mathbf{m}_{\text{quad}} = \frac{3}{40} L^2 \left(\beta_1^2 + \frac{\beta_2^4 + \beta_1 \beta_2^3}{\beta_1^2 + \beta_1 \beta_2 + \beta_2^2} - \frac{5}{3} \right) \mathbf{m}. \quad (7)$$

The values of β_1 and β_2 that set (7) to zero correspond to geometries with minimal dipole-field approximation error. Letting $\beta_1 = \alpha\beta_2$ and substituting into the polynomial in (7) and setting to zero gives an alternate equation for zero quadrupole moments:

$$3\beta_2^4(\alpha^4 + \alpha^3 + \alpha^2 + \alpha + 1) - 5\beta_2^2(\alpha^2 + \alpha + 1) = 0 \quad (8)$$

Inspection of (8) shows there is no quadrupole moment when $\beta_1 = \beta_2 = 0$ (no magnet), when $\beta_1 = \beta_2 = \alpha = 1$ (thin walled shell), and when $\beta_1 = 0, \beta_2 = \sqrt{5/3}, \alpha = 0$ (no inner hole). As the definition of β_1 and β_2 requires $\beta_1 \leq \beta_2$, the only physically meaningful solutions to (8) lie in the range $\beta_1 \in (0, 1)$ and $\beta_2 \in (1, \sqrt{5/3})$, which correspond to geometries that are shorter than they are wide ($L < W + 2T$). A fit of the roots of (8) can be used to provide an approximation of the relationship between β_1 and β_2 :

$$\beta_2 \approx ((5/3)^{n/2} - \beta_1^n)^{1/n} \quad (0 \leq \beta_1 \leq 1) \quad (9)$$

$$n = \frac{2 \log 2}{\log(5/3)} \approx 2.714$$

which provides solutions to (8) accurate to within 0.17% over the range $\beta_1 \in (0, 1)$.

B. Core Dipole-Field Contribution

Since the core is spherical and placed in the nearly uniform field inside of the solenoid, it is assumed that it will magnetize uniformly and contribute a pure dipole field (it was verified numerically *post facto* that the root-mean-squared deviation in the magnetization was less than 7% of the mean).

The dipole moment of a low-coercivity, low-remnance, and high-permeability ($\chi \gg 1$) spherical core, when magnetized in its linear region (i.e., below magnetic saturation), is

$$\mathbf{m}_c = \overline{\mathbf{M}} \mathcal{V}_c = \left(\frac{\chi}{1 + \frac{1}{3}\chi} \frac{\overline{\mathbf{B}}}{\mu_0} \right) \left(\frac{4\pi}{3} R_c^3 \right) \approx \frac{4\pi R_c^3}{\mu_0} \mathbf{B}_c \quad (10)$$

where R_c is the radius of the core, \mathbf{M} is the magnetization in units $\{\text{A}\cdot\text{m}^{-1}\}$, the overbar represents a quantity averaged over the core volume \mathcal{V}_c , and \mathbf{B}_c is the applied magnetic field at the center of the core, which is a linear combination of the field due to each solenoid. The applied field from each square-cross-section solenoid with uniform current density J , length L , and axis $\hat{\mathbf{l}}$, calculated by the Biot-Savart law, is:

$$\mathbf{B}_c = \frac{2LJ\mu_0}{\pi} \int_{\beta_1}^{\beta_2} \text{atan} \left(\frac{1}{\sqrt{1+2\zeta^2}} \right) d\zeta \hat{\mathbf{l}}. \quad (11)$$

By combining the dipole moments due to the magnetized core and each of the solenoids, the total dipole moment of the Omnimaget $\mathbf{m} = \mathbf{m}_x + \mathbf{m}_y + \mathbf{m}_z$ is thus:

$$\begin{aligned} \mathbf{m} &= \sum_{i \in \{x, y, z\}} J_i \left(8L_i R_c^3 \int_{\beta_{i,1}}^{\beta_{i,2}} \text{atan} \left(\frac{1}{\sqrt{1+2\zeta^2}} \right) d\zeta \right. \\ &\quad \left. + \frac{L_i^4}{6} (\beta_{i,2}^3 - \beta_{i,1}^3) \right) \hat{\mathbf{l}}_i \\ &= \mathbb{M} \begin{bmatrix} J_x A_{w,x} \\ J_y A_{w,y} \\ J_z A_{w,z} \end{bmatrix} = \mathbb{M} \mathbf{I} \end{aligned} \quad (12)$$

where the indices x, y , and z correspond to the inner, middle, and outer solenoids, respectively and without loss of generality, A_w is the conductor (e.g., wire) area used to wind the solenoid, and \mathbb{M} is a linear transformation that maps the three applied currents in the array \mathbf{I} to the dipole moment \mathbf{m} . Since the matrix \mathbb{M} is only a function of the solenoids' geometries, the optimization problem can be split into four steps: choose the maximum current densities \mathbf{I}_{max} in each direction based on thermal or amplifier constraints, determine the geometric β factors to equalize the components of $\mathbb{M} \mathbf{I}_{\text{max}}$, optimize the overall size to a set of physical and operational constraints (e.g., field strength, field gradient, weight, electrical time constant), and finally tailor the wire gage for manufacturability or amplifier voltage/current limitations.

C. Dipole Moment Equalization

The optimal geometry for the Omnimaget corresponds to the geometric ratios that maximize the dipole moment generated in each direction, have the same ratio of dipole moment to maximum current density in each direction, and have no quadrupole moment. This is a constrained optimization problem, and can be non-dimensionalized by dividing all of the lengths by L_{max} (the edge length of a minimum-bounding cube) and the moments by $m_{\text{ref}} = J_{\text{max}} L_{\text{max}}^4/18$ (the maximum no-ferromagnetic-material dipole moment introduced earlier). The constraints can be simplified because, from (7), the length of each solenoid must be shorter than its outer width. Thus,

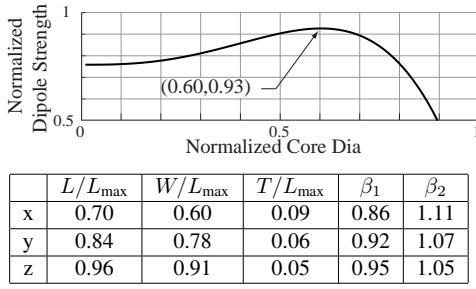


Fig. 2. The optimal geometry for a no-quadrupole Omnimaget. The dipole moments have been normalized by $JL_{\max}^4/18$ and have a maximum at a core-diameter-to-outer-Omnimaget-dimension ratio $2R_c/L_{\max} = 0.60$. The table provides the geometric ratios that describe the shape of the three nested solenoids that correspond to this optimal configuration. All length parameters are normalized by the outer Omnimaget cubic length L_{\max} .

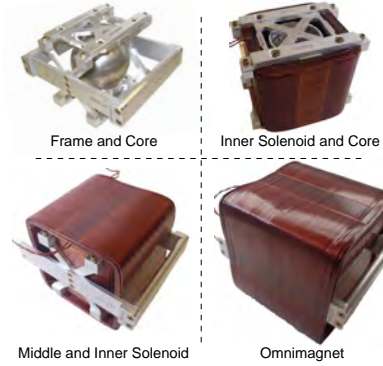
the objective is to maximize the dipole moment magnitude $\|\mathbf{m}\|$ subject to:

- Eq.(7) equals zero (i.e., the configuration has no quadrupole moment).
- $\|\mathbf{m}_x\|/m_{\text{ref}} = \|\mathbf{m}_y\|/m_{\text{ref}} = \|\mathbf{m}_z\|/m_{\text{ref}}$ (i.e., omnidirectionality).
- $W_x = 2R_c$ (i.e., the core diameter is the same as the inner solenoid's inner width).
- $W_y = W_x + 2T_x$ (i.e., the inner solenoid's outer width is the same size as the middle solenoid's inner width).
- $W_z = W_y + 2T_y$ (i.e., the middle solenoid's outer width is the same size as the outer solenoid's inner width).

This optimization is performed using R_c as the free parameter (Fig. 2). There is a maximum that occurs when the core diameter is 60% of L_{\max} . Although the magnitude of the dipole moment in each direction is the same for the same applied current, the percentages of the dipole moment attributed to the core or the windings are different for each solenoid; the percentage of the dipole moment from the core/windings is 41/59, 28/72, and 21/79 for the inner, middle, and outer solenoids, respectively. The optimized configuration has dipole-moment magnitudes that are 93% of what could be theoretically expected with no ferromagnetic material and no voids (an unrealizable geometry), and 22% greater than the realizable geometry of three nested solenoids with no ferromagnetic core (but with significantly less power consumption and more heat-transfer surface area). The optimal design's dipole moment is:

$$\begin{aligned} \mathbf{m} &= 61.86 \times 10^{-3} L_z^4 \mathbf{J} \\ &= 51.45 \times 10^{-3} L_{\max}^4 \mathbf{J} \end{aligned} \quad (13)$$

Solutions to the right of the maximum in Fig. 2 correspond to geometries with more inert (i.e., non-current-energized) material and will produce less heat and require less power than the corresponding geometry to the left of the optimal point. The flatness of the maximum indicates that variations about the optimal point will not substantially affect the performance of the resulting Omnimaget. Fortunately, the solenoids are shorter than they are wide, which allows paths for conductors and coolant to reach the middle and inner solenoids, making the implementation of this design feasible.



	L (mm)	W (mm)	T (mm)	β_1	β_2
x	120	103	16	0.86	1.12
y	149	137	11	0.92	1.07
z	170	160	8	0.95	1.05

Fig. 3. The assembled Omnimaget used in the testing described in this paper. The core used is 100mm, which is 57% of $L_{\max} = 176$ mm. The deviations from Fig. 2 are due to reoptimizing with 1mm air-gaps between the components for assembly.

D. Prototype

An Omnimaget was constructed using a 100mm diameter spherical Nickel-Iron (ASTM A753-08-K94840) core. The core material was chosen because it has a high magnetic permeability, a low magnetic remanence, and a low magnetic coercivity (i.e., it magnetizes easily but does not remain magnetized when the magnetizing field is removed). The solenoids were constructed using 16AWG square self-bonding copper wire from MWS Wire Industries Inc. The optimization was repeated including a 1mm spacing between each of the components for assembly. The slightly modified optimization did not change the shape of the coils substantially but shifted the optimal core size to 57% of the edge length of the minimum-bounding cube, which is $L_{\max} = 176$ mm. The additional empty space also reduced the overall strength of the design from 93% to 87% of m_{ref} . Because of the quantization in lengths and widths inherent with any winding, the constructed Omnimaget has slight variations in the dipole-moment strengths of each solenoid and has successfully minimized, but not eliminated, the quadrupole term ($\mathbf{m}_{\text{quad}} \approx 0.04\mathbf{m}$). The prototype constructed is shown in Fig. 3, with the table providing its dimensions; the dipole-moment per conductor-current is calculated to be 25.1, 25.8, and 26.3 ($\text{A} \cdot \text{m}^2$)/A for the inner, middle, and outer solenoids, respectively, which form the diagonal entries of \mathbf{M} . The field at the surface with 1A applied is measured to be 5.6, 4.7, and 3.6 mT for the inner, middle, and outer solenoids, respectively; at 12cm from the surface the field is 0.6mT for each. The inductance for each solenoid in the assembled Omnimaget was measured to be 120, 107, and 78 mH for the inner, middle, and outer solenoids, respectively.

Since each solenoid in the Omnimaget has a different geometry, the magnetic field produced by each solenoid will

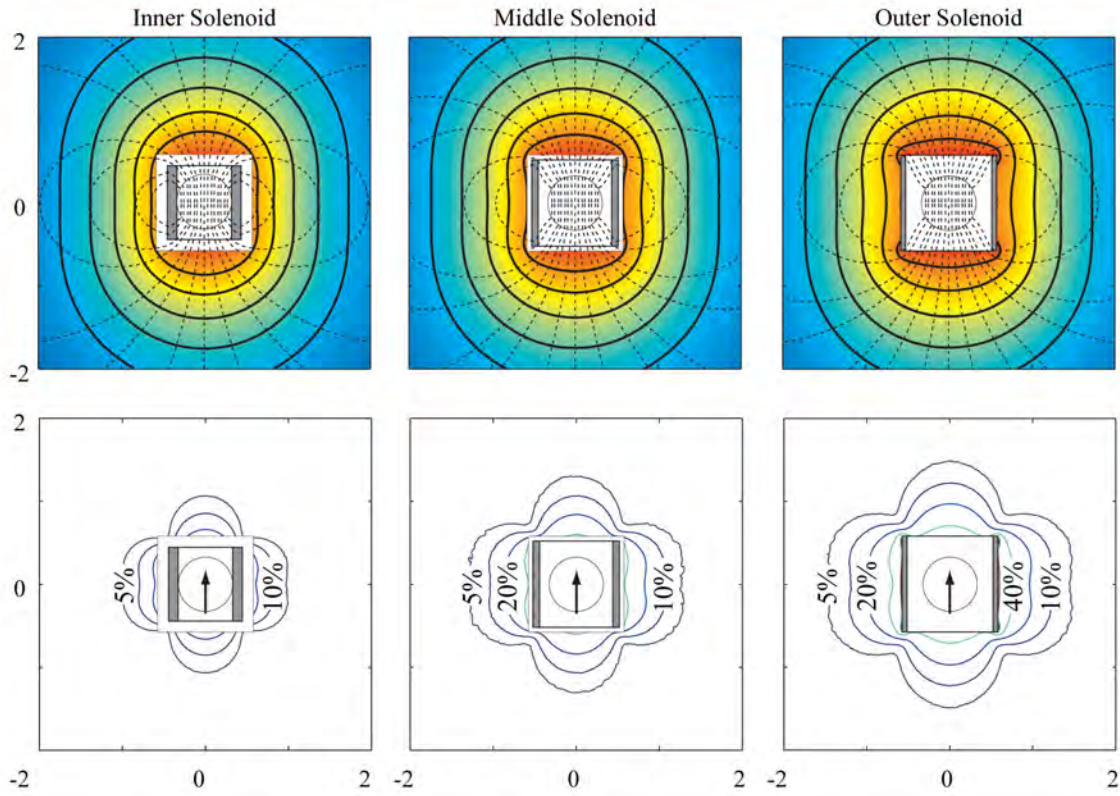


Fig. 4. The field shape (top, dotted) and magnitude (top, solid and color contour), and field error relative to the dipole approximation (bottom) are shown. The distances are normalized by the radius of a minimum-bounding sphere: $(\sqrt{3}/2) L_{\max}$. In the top row, the innermost contour line corresponds to $\|\mathbf{B}\| = 64\mu_0 \|\mathbf{m}\|$, and each successively larger contour corresponds to a halving in field magnitude, with the outermost contour corresponding to $\|\mathbf{B}\| = 4\mu_0 \|\mathbf{m}\|$.

not have exactly the same shape for positions close to the Omnimaget. To understand the subtle differences in field shape, FEA simulations were performed using Ansoft Maxwell 14.0. Since the core is magnetized in the linear region and the solenoids are orthogonal, solenoid-solenoid magnetic coupling is negligible, so in these simulations only one of the solenoids is energized at a time. The results of the simulation (field strength, field shape, and percent error from the point-dipole approximation) for each solenoid are shown in Fig. 4. As the outermost solenoid is the largest, it is responsible for the majority of the field deviations close to the Omnimaget. The field in each direction rapidly reduces to a pure dipole field with distance; the deviations are comparable to non-spherical permanent magnets [21].

III. EFFECT OF ADJACENT MAGNETIC SOURCES

Because the Omnimaget contains a spherical ferromagnetic core, any adjacent magnetic source (e.g., a permanent magnet used in a magnetic tool) will slightly magnetize the core, causing the resulting dipole moment of the Omnimaget to be perturbed. The effect of the external field on the core is given by (10) where $\mathbf{B}_c = \mathbf{B}_{c,p}$ is given by the value of the external

field that is perturbing the magnetization at the center of the core. Due to the linearity of the magnetics equations when the core is unsaturated, the resulting Omnimaget dipole moment is the sum of the original desired moment and the perturbed moment:

$$\mathbf{m} = \mathbf{M}\mathbf{I} + \frac{4\pi R_c^3}{\mu_0} \mathbf{B}_{c,p} \quad (14)$$

To account for perturbing field sources, it is necessary to subtract their effect from the desired dipole moment prior to calculating the currents required.

IV. PHYSICAL PROPERTIES

The primary design of an Omnimaget is focused on the optimization of its magnetic properties. However, any physical system will have to be designed around other limitations such as weight, electrical resistance, electrical inductance, and heating limits.

A. Weight

The weight of the Omnimagnet is purely a function of volume:

$$W = \rho_{\text{core}} \frac{4\pi R_c^3}{3} + \rho_s \sum_{i \in \{x, y, z\}} L_i^3 (\beta_{i,2}^2 - \beta_{i,1}^2) \quad (15)$$

where ρ_{core} and ρ_s are the densities of the core and solenoid material, respectively, in units (kg·m⁻³).

B. Resistance and Heating/Cooling Limits

The electrical resistance of each solenoid is a function of both the volume and the wire size chosen:

$$R = \frac{\rho_w \eta L^3}{A_w^2} (\beta_2^2 - \beta_1^2) \quad (16)$$

where ρ_w is the resistivity of the wire in units (Ω·m), A_w is the cross-sectional area of the conductor used, and η describes the packing density of the conductor (1 for square wire and $\pi/4$ for round wire). The resistance of the Omnimagnet system can be described by the diagonal matrix \mathbb{R} , which is formed by packing each coil's resistance along the diagonal. With this definition the power lost to Joule heating becomes:

$$\dot{q}_{\text{gen}} = \mathbf{I}^T \mathbb{R} \mathbf{I} \quad (17)$$

For the Omnimagnet to be operating at thermal equilibrium, the heat generated $\dot{q}_{i,\text{gen}}$ must be balanced by the heat conducted or convected from the coil to the environment via a fluid (e.g., air, transformer oil). The heat transfer rate is a function of surface area and temperature difference:

$$\dot{q}_{i,\text{out}} = 2h_i L_i^2 (\beta_{i,2}^2 - \beta_{i,1}^2 + 2(\beta_{i,2} + \beta_{i,1})) \Delta T_i \quad (18)$$

where h describes the total heat transfer coefficient and ΔT is the temperature difference between the coil and the environment. The equilibrium temperature is reached when the heat generated by Joule heating is balanced by the heat convected out of the system, which determines the maximum current density:

$$J_{i,\text{max}} = \sqrt{\frac{h_i \Delta T_i}{L_{\text{max}} \rho_w} \frac{2(\beta_{i,2}^2 - \beta_{i,1}^2 + 2(\beta_{i,2} + \beta_{i,1}))}{(L_i/L_{\text{max}})(\beta_{i,2}^2 - \beta_{i,1}^2)}} \quad (19)$$

From the definition of the Nusselt number and assuming forced convection in a channel, we have $h \propto L^{-1}$, which implies $J_{\text{max}} \propto L_{\text{max}}^{-1}$. The maximum dipole moment that can be generated is thus:

$$\mathbf{m}_{\text{max}} = \mathbb{M} \mathbf{J}_{\text{max}} \propto L_{\text{max}}^3 \quad (20)$$

which is the same scaling as would be expected for a permanent magnet. The magnetic field generated scales homothetically and the field gradients, which are proportional to the force applied to an adjacent magnet, scale inversely with L_{max} .

C. Inductance and Time Constant

The inductances, and therefore time constants, of the Omnimagnet solenoids are difficult to calculate exactly because of their shape and the presence of the spherical core. However, an approximation can be derived that will suffice for use in Omnimagnet design. The approach separates the problem into two parts: the inherent inductance in the solenoid due to the windings, and the additional inductance due to the spherical core. As shown in the derivation provided in the Appendix, the inductance \mathcal{L} can be written as a function of relative solenoid shape scaled by a function of solenoid size.

$$\mathcal{L} \approx \frac{\mu_0 \eta L^5}{6\pi A_w^2} f_1(\beta_1, \beta_2, \beta_c), \quad (21)$$

$$\begin{aligned} f_1(\beta_1, \beta_2, \beta_c) &= (\beta_2^3 - \beta_1^3) \int_{-1/2}^{1/2} \int_{\beta_1}^{\beta_2} f_2(\zeta_1, \zeta_2) d\zeta_1 d\zeta_2 \\ &\quad + \pi \beta_c^3 (\beta_2 - \beta_1) \int_{\beta_1}^{\beta_2} f_2(\zeta_1, 0) d\zeta_1 \\ f_2(\zeta_1, \zeta_2) &= \arctan \left(\frac{1 + 2\zeta_2}{\sqrt{(1 + 2\zeta_2)^2 + 2\zeta_1^2}} \right) \\ &\quad + \arctan \left(\frac{1 - 2\zeta_2}{\sqrt{(1 - 2\zeta_2)^2 + 2\zeta_1^2}} \right) \end{aligned}$$

where β_c is the ratio of core diameter to solenoid length. The calculated inductances for the as-built configuration are 163, 110, and 82 mH, for the inner, middle, and outer solenoids respectively. This is within 35% of the measured values reported above, indicating reasonable agreement between the approximation and the measurement. The values of f_1 for the optimal geometry defined earlier are 0.372, 0.089, and 0.037 for the inner, middle, and outer solenoids, respectively.

The time constant τ for each solenoid is:

$$\tau = \frac{\mathcal{L}}{R} \approx L^2 \frac{\mu_0}{2\pi \rho_w} \frac{f_1(\beta_1, \beta_2, \beta_c)}{\beta_2^2 - \beta_1^2} \quad (22)$$

Although the system resistance and inductance can be tailored through wire selection, the time constant is independent of wire choice. Since the equations for time constant and dipole moment are functions of the same variables, it is not possible to design the two properties independently.

V. FIELD CONTROL

Fundamentally, the Omnimagnet is a magnetic field source with three control inputs (the current applied to each solenoid), which can be used to generate a desired magnetic field at a location in space. Since the magnetic field generated is closely represented by a dipole field, at each location in space it will produce both a field and spatial derivatives in the field. With a single Omnimagnet with three degrees of freedom, it is not possible to independently control field and field gradient simultaneously.

To determine the dipole moment \mathbf{m} required by the Omnimagnet to produce a desired field \mathbf{B} at some point \mathbf{p} , the vector dipole equation (3) must be inverted. Using the dipole

field analysis in [12], it can be shown that the inverse exists of the form:

$$\mathbf{m} = \frac{2\pi}{\mu_0} \|\mathbf{p}\|^3 (3\hat{\mathbf{p}}\hat{\mathbf{p}}^T - 2\mathbf{I}) \mathbf{B} \quad (23)$$

Combining with (12), the currents required are thus:

$$\mathbf{I} = \frac{2\pi}{\mu_0} \|\mathbf{p}\|^3 \mathbf{M}^{-1} (3\hat{\mathbf{p}}\hat{\mathbf{p}}^T - 2\mathbf{I}) \mathbf{B} \quad (24)$$

VI. REMOTE MANIPULATION WITH AN OMNIMAGNET

At steady-state, the torque applied by a magnetic field on a magnetic tool will tend to align the tool with the field. This can be used to reduce the control problem from controlling torque directly, and thus requiring both tool orientation and position, to controlling field directly, and thus requiring only tool position. Controlling the propulsion of a ball or helical screw with this approach has been explored using a rotating permanent magnet [12]. However, when a permanent magnet is used to create a rotating field, both the magnitude and rotation rate of the field vary elliptically at the tool location; thus, the rotational speed of the permanent magnet needs to be constantly updated in order to produce a constant tool rotation rate [12]. Since the Omnimaget can produce a desired field at a specific point in space, it is possible to create a rotating field with angular velocity ω without the elliptical modulation in magnitude associated with rotating permanent magnets. This can be accomplished by updating the desired \mathbf{B} in (24) as

$$\mathbf{B}[k+1] = e^{\mathbf{S}(\omega\Delta t)} \mathbf{B}[k] \quad (25)$$

where Δt is the time step of the control system and the matrix exponential of a skew-symmetric matrix creates a rotation matrix [22]. Thus, the same steady-state rotating control approaches can be performed by an Omnimaget using (24) and (25) in which, unlike permanent magnets, both the desired field magnitude and orientation are specified.

A rotating magnetic field was used to propel a threaded capsule endoscope mockup down a transparent lumen, which was offset by 120 mm from the surface of the Omnimaget, as shown in Fig. 5. Although the trajectory of the capsule is simple (a line), the translating rotational field necessary to drive the capsule uses all three degrees of freedom available to the Omnimaget. The desired magnetic field with $\|\mathbf{B}\|=3$ mT was updated using (25) for a rotational rate of 4π rad \cdot s $^{-1}$. The position of the capsule was tracked using a stereo-vision system, although other localization methods, such as the magnetic localization of [20], could be used in the future. This position was used in conjunction with (24) to calculate the currents necessary to produce the desired field at the location of the capsule. The necessary currents were controlled by a DC voltage signal sent from a Sensoray S626 controller card to Advanced Motion Control AMC16A8 current drives at an update rate of $\Delta t = 0.01$ s.

VII. DISCUSSION

The Omnimaget prototype developed in this paper uses no form of forced cooling. However, for Omnimagets to be truly effective, they will need to be cooled. Immersive

fluid cooling and forced-convection fluid cooling will enable higher currents, and therefore higher fields, to be generated. An Omnimaget's dipole strength also increases with size, but this must be balanced against an increase in cost and weight.

By combining multiple Omnimagets together, it will be possible to create more sophisticated magnetic manipulation systems. For example, the Octomag system uses eight stationary electromagnets to generate 3-DOF force and 2-DOF torque on magnetic devices [7]. A system consisting of three Omnimagets is essentially nine stationary electromagnets, meaning that similar levels of control as the Octomag seem conceivable. The commercial Stereotaxis Niobe system uses two large orientation-controlled permanent magnets to steer magnetic catheters. A system consisting of two Omnimagets has the ability to recreate the same type of magnetic control. Additionally, the spherical core inside the Omnimaget makes its use in multi-Omnimaget systems extremely promising. Because the average magnetization of a spherical core can be solved using only knowledge of the applied field at the center of the sphere, it will be possible to solve for the combined field of multiple Omnimagets analytically, rather than relying on *in situ* system calibration.

If an Omnimaget were constructed with a cubic core, the available ferromagnetic material would increase by 57%, which suggests that the overall strength of the magnet would increase. Using the methodology outlined in this paper, preliminary simulations indicate that the dipole moment of an equivalently sized Omnimaget with a cubic core would be about 115% of the no-ferromagnetic-material reference geometry, which is 24% stronger than the optimal spherical-core geometry. Because the core is no longer spherical, this additional strength is also associated with larger dipole-modeling errors (equivalent to the errors associated with cubic permanent magnets [21]) and a significantly more complicated core magnetization calculation. If multiple Omnimagets were to be used in concert, the complexity of the mutual magnetization could be prohibitive, requiring *in situ* calibration. However, if only one Omnimaget is required for the application, a single Omnimaget with a cubic core could provide a significant increase in strength with only a marginal increase in reoptimization and development complexity.

VIII. CONCLUSIONS

The design and optimization of an Omnimaget was provided. The realized version of the design has an optimal core-radius to outer-length ratio of 0.57 and can achieve field strengths that are 87% of the unrealizable theoretical reference. The design was optimized to create a dipole-like field with the error relative to the dipole model falling to below 5% outside of 1.5 minimum-bounding-sphere radii from the center. Manipulation with the Omnimaget was demonstrated by actuating a helical capsule down a lumen. Not only can the Omnimaget create a rotating dipole field like a permanent magnet, but it can also control the field strength like a standard electromagnet. This enables new control methodologies to be explored. Moreover, the spherical core will allow the combined field of multiple Omnimagets to be solved analytically.

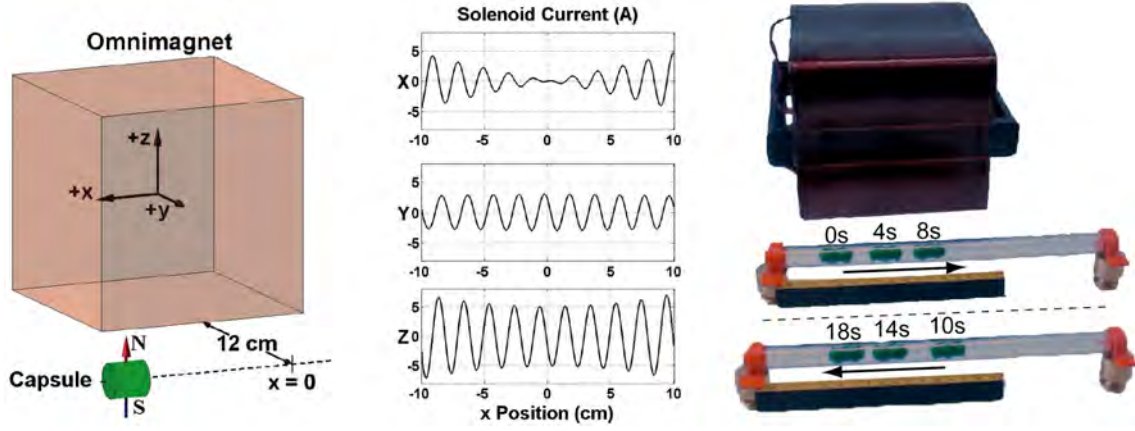


Fig. 5. Propulsion of a helical capsule at $10 \text{ mm} \cdot \text{s}^{-1}$ through a lumen located 120 mm from the surface of the Omnimagnet, which is applying a rotating magnetic field at the location of the helical capsule. (left) Numerical simulation with (center) resulting solenoid currents. (right) Experimental demonstration with a capsule mockup.

APPENDIX

This appendix provides the derivation of the approximate inductance of a square-cross-sectional solenoid with a spherical core. The magnetic flux Φ through a current loop is related to the inductance of the loop \mathcal{L} by:

$$\Phi \equiv \int \mathbf{B} \cdot d\mathbf{a} = \mathcal{L}I \quad (26)$$

where $d\mathbf{a}$ is the differential area of the plane inside the loop [18]. It should be noted that if the Omnimagnet's solenoids are mutually orthogonal, the mutual inductance between each solenoid is zero because of the dot product in (26). Thus, the inductance of a collection of connected loops is:

$$\mathcal{L} = \sum_{i=1}^N \frac{\Phi_i}{I} \quad (27)$$

where N is the total number of loops. Letting η be the area packing efficiency of the wire, the total number of loops can be obtained geometrically:

$$N = \frac{\eta TL}{A_w} = \frac{\eta(\beta_2 - \beta_1)L^2}{2A_w} \quad (28)$$

Although possible, computing the sum in (27) is cumbersome. If, instead of summing fluxes and loops in the solenoid, we integrate an effective flux and cross-sectional loop density over the solenoid, the computation of the inductance can be greatly simplified. The loop density, gleaned by inspection of (28), is η/A_w . Thus, in terms of an effective loop density the total number of loops is:

$$N = \int dN = \int_{-L/2}^{L/2} \int_0^T \frac{\eta}{A_w} dT dL \quad (29)$$

Keeping with the theme of non-dimensionalizing the geometric lengths, we use the change of variable $dT = Ld\zeta_T$ and $dL =$

$Ld\zeta_L$. With this substitution we obtain:

$$N = \int_{-1/2}^{1/2} \int_0^{\frac{(\beta_2 - \beta_1)}{2}} \frac{\eta L^2}{A_w} d\zeta_T d\zeta_L \quad (30)$$

and (27) can be approximated as:

$$\mathcal{L} \approx \frac{\eta L^2}{IA_w} \int_{-1/2}^{1/2} \int_0^{\frac{(\beta_2 - \beta_1)}{2}} \Phi(\zeta_T, \zeta_L) d\zeta_T d\zeta_L \quad (31)$$

It is now left to define the effective flux density in the solenoid $\Phi(\zeta_T, \zeta_L)$. Referring to (26), the flux density is formed by an area component and a field component. The area associated with the loop density can be obtained geometrically and is $L^2(2\zeta_T + \beta_1)^2$; the loop-density flux is therefore:

$$\Phi(\zeta_T, \zeta_L) = L^2(2\zeta_T + \beta_1)^2 \mathcal{B}(\zeta_T, \zeta_L) \quad (32)$$

The magnetic field $\mathcal{B}(\zeta_T, \zeta_L)$ associated with the loop-density flux is the average field within the differential loop, which is difficult to calculate exactly but will be simplified with another approximation.

Without loss of generality, we will take the axis of the solenoid to be oriented in the cartesian z direction. The calculation of $\mathcal{B}(\zeta_T, \zeta_L)$ is simplified by assuming the field inside the solenoid when no core is present $\mathcal{B}_s(z)$ varies along the solenoid axis but is constant across the cross-section.

$$\mathcal{B}_s(z) = \frac{LJ\mu_0}{\pi} \int_{\beta_1}^{\beta_2} \left(\text{atan} \left(\frac{1 + 2z/L}{\sqrt{(1 + 2z/L)^2 + 2\zeta^2}} \right) + \text{atan} \left(\frac{1 - 2z/L}{\sqrt{(1 - 2z/L)^2 + 2\zeta^2}} \right) \right) d\zeta \quad (33)$$

Note that (33) reduces to (11) when $z = 0$. Since we are magnetizing the spherical core in its linear region, the field is the superposition of the field from only the solenoid current

$\mathcal{B}_s(L\zeta_L)$ and the field only from the magnetization of the core $\mathcal{B}_c(\zeta_T, \zeta_L)$; thus, $\mathcal{B}(\zeta_T, \zeta_L) \approx \mathcal{B}_s(L\zeta_L) + \mathcal{B}_c(\zeta_T, \zeta_L)$. With this simplification, the inductance due to the solenoid with a core can be split into two separate problems: the inductance of a solenoid with no core and the inductance due only to the magnetization of the core.

Using (31), (32), and (33), the inductance for a square solenoid with no core is:

$$\begin{aligned} \mathcal{L}_s &\approx \frac{\eta L^4}{A_w I} \int_{-1/2}^{1/2} \int_0^{\beta_2 - \beta_1} (\beta_1 + 2\zeta_T)^2 \mathcal{B}_s(L\zeta_L) d\zeta_T d\zeta_L \\ &\approx \frac{\eta L^4 (\beta_2^3 - \beta_1^3)}{6A_w I} \int_{-1/2}^{1/2} \mathcal{B}_s(\zeta_L L) d\zeta_L \end{aligned} \quad (34)$$

The inductance contribution of the core is more difficult to calculate; but, the calculation can be split into two parts as well: that which is associated with the uniform field inside the core, and that which is associated with the dipole field outside the core.

Inside of a uniformly magnetized spherical core, the magnetic field due only to the magnetization of the material is uniform and is [18]:

$$\mathcal{B}_{c,i} = \frac{2}{3} \mu_0 \|\mathbf{M}\| = 2\mathcal{B}_s(0) \quad (35)$$

When the magnetization is due to an external field, the total internal field is then $2\mathcal{B}_s(0) + \mathcal{B}_s(0) = 3\mathcal{B}_s(0)$, which is expected since the demagnetization factor of a sphere is $1/3$. Since the external field is already accounted for in the solenoid-alone inductance, the field of $2\mathcal{B}_s(0)$ will be used to calculate the part of the inductance only due to magnetizing the core material. The inductance associated with the field inside the core is thus:

$$\begin{aligned} \mathcal{L}_{c,i} &= \frac{\eta L^4 (\beta_2 - \beta_1)}{2A_w I} \int_{-\beta_c/2}^{\beta_c/2} \pi (\beta_c^2/4 + \zeta_1^2) \mathcal{B}_s(0) d\zeta \\ &= \frac{\pi \eta L^4 (\beta_2 - \beta_1) \beta_c^3 \mathcal{B}_s(0)}{6A_w I} \end{aligned} \quad (36)$$

where β_c is being introduced as the ratio of core diameter to solenoid length.

Outside of the magnetized core, the field is purely dipolar with the dipole moment given by (10). To numerically determine the inductance of this field, the differential flux is given by:

$$\frac{d\Phi}{da} = \frac{\mu_0 \|\mathbf{m}\|}{4\pi \|\mathbf{p}\|^3} \hat{\mathbf{z}}^T (3\hat{\mathbf{p}}\hat{\mathbf{p}}^T - \mathbb{I}) \hat{\mathbf{z}} = \frac{L^3 \beta_c^3 \mathcal{B}_s(0)}{8 \|\mathbf{p}\|^3} (3(\hat{\mathbf{z}}^T \hat{\mathbf{p}})^2 - 1) \quad (37)$$

The inductance is given by (31) where the flux is the flux outside of the core and inside of the loop-density width being integrated:

$$\begin{aligned} \mathcal{L}_{c,dipole} &= \\ &\frac{\eta \beta_c^3 L^4}{8A_w I} \mathcal{B}(0) \iiint \left(\frac{2(\zeta_L L)^2 - x^2 - y^2}{(x^2 + y^2 + (\zeta_L L)^2)^{5/2}} \right) dx dy d\zeta_T d\zeta_L \end{aligned} \quad (38)$$

Numerical analysis of this contribution indicates it accounts for less than 2% of the total inductance and will be neglected for simplicity.

Therefore, the total inductance is the combination of the inductance due to the solenoid alone, plus the inductance due to uniform field inside of the magnetized core:

$$\begin{aligned} \mathcal{L} &\approx \frac{\eta L^4}{6A_w I} (\beta_2^3 - \beta_1^3) \int_{-1/2}^{1/2} \mathcal{B}_s(\zeta_L L) d\zeta_L \\ &\quad + \frac{\eta L^4}{6A_w I} \pi (\beta_2 - \beta_1) \beta_c^3 \mathcal{B}_s(0) \end{aligned} \quad (39)$$

Combining (33) and (39), this inductance can be rewritten as a function of relative solenoid shape scaled by a function of solenoid size as shown in (21), where $f_1(\cdot)$ is the integration described in (39) with $f_2(\cdot)$ comprising the integrand of (33).

ACKNOWLEDGMENT

This material is based upon work supported by the National Science Foundation under Grant Nos. 0952718 and 0654414.

REFERENCES

- [1] T. Honda, K. I. Arai, and K. Ishiyama, "Micro swimming mechanisms propelled by external magnetic fields," *IEEE Trans. Magn.*, vol. 32, no. 5, pp. 5085–5087, 1996.
- [2] D. Meeker, E. H. Maslen, R. C. Ritter, and F. Creighton, "Optimal realization of arbitrary forces in a magnetic stereotaxis system," *IEEE Trans. Magn.*, vol. 32, no. 2, pp. 320–328, 1996.
- [3] M. Sendoh, K. Ishiyama, and K. Arai, "Direction and individual control of magnetic micromachine," *IEEE Trans. Magn.*, vol. 38, no. 5, pp. 3356–3358, 2002.
- [4] H. Lee, A. Purdon, and R. M. Westervelt, "Micromanipulation of biological systems with microelectromagnets," *IEEE Trans. Magn.*, vol. 40, no. 4, pp. 2991–2993, 2004.
- [5] S. Martel, C. C. Tremblay, S. Ngakeng, and G. Langlois, "Controlled manipulation and actuation of micro-objects with magnetotactic bacteria," *Appl. Phys. Lett.*, vol. 89, no. 233904, pp. 1–3, 2006.
- [6] S. Martel, J.-B. Mathieu, O. Felfoul, A. Chanu, E. Aboussouan, S. Tamaz, P. Pouponneau, L. Yahia, G. Beaudoin, G. Soulez, and M. Mankiewicz, "Automatic navigation of an untethered device in the artery of a living animal using a conventional clinical magnetic resonance imaging system," *Appl. Phys. Lett.*, vol. 90, no. 114105, pp. 1–3, 2007.
- [7] M. P. Kummer, J. J. Abbott, B. E. Kratochvil, R. Borer, A. Sengul, and B. J. Nelson, "Octomag: An electromagnetic system for 5-dof wireless micromanipulation," *IEEE Trans. Robot.*, vol. 26, no. 6, pp. 1006–1017, 2010.
- [8] M. Mehrtash, N. Tsuda, and M. Khamesee, "Bilateral macro-micro teleoperation using magnetic levitation," *IEEE-ASME Trans. Mech.*, vol. 16, no. 3, pp. 459–469, 2011.
- [9] M. H. Hagiwara, T. K. Kawahara, Y. Yamanishi, and F. Arai, "Driving method of microtool by horizontally arranged permanent magnets for single cell manipulation," *Appl. Phys. Lett.*, vol. 97, no. 013701, pp. 1–3, 2010.
- [10] G. Ciuti, P. Valdastrì, A. Menciassi, and P. Dario, "Robotic magnetic steering and locomotion of capsule endoscope for diagnostic and surgical endoluminal procedures," *Robotica*, vol. 28, pp. 199–207, 2010.
- [11] S. Yim and M. Sitti, "Design and rolling locomotion of a magnetically actuated soft capsule endoscope," *IEEE Trans. Robot.*, vol. 28, no. 1, pp. 183–194, 2012.
- [12] A. W. Mahoney, D. L. Cowan, K. M. Miller, and J. J. Abbott, "Control of untethered magnetically actuated tools using a rotating permanent magnet in any position," *IEEE Int. Conf. Robotics and Automation*, 2012.
- [13] S. Ernst, F. Ouyang, C. Linder, K. Hertting, F. Stahl, J. Chun, H. Hachiy, D. Bansch, M. Antz, and K.-H. Kuck, "Initial experience with remote catheter ablation using a novel magnetic navigation system magnetic remote catheter ablation," *Circulation*, vol. 109, no. 12, pp. 1472–1475, 2004.

This is the author's version of an article that has been published in this journal. Changes were made to this version by the publisher prior to publication.
The final version of record is available at <http://dx.doi.org/10.1109/TMAG.2014.2303784>

TRANSACTIONS ON MAGNETICS, VOL. ??, NO. ??, ?? 2013

10

- [14] A. W. Mahoney and J. J. Abbott, "Managing magnetic force applied to a magnetic device by a rotating dipole field," *Appl. Phys. Lett.*, vol. 99, no. 134103, pp. 1–3, 2011.
- [15] F. Raab, E. Blood, T. Steiner, and H. Jones, "Magnetic position and orientation tracking system," *IEEE Tran. Aerospace and Electronic Systems*, vol. AES-15, no. 5, pp. 709–718, Sept. 1979.
- [16] R. Carta, J. Thoné, and R. Puers, "A wireless power supply system for robotic capsular endoscopes," *Sens. Actuators, A*, vol. 162, no. 2, pp. 177–183, 2010.
- [17] A. J. Petruska and J. J. Abbott, "An omnidirectional electromagnet for remote manipulation," in *IEEE Int. Conf. Robotics and Automation*, 2013, pp. 814–819.
- [18] D. J. Griffiths, *Introduction to Electrodynamics*. Prentice Hall, 1999.
- [19] A. W. Mahoney, S. E. Wright, and J. J. Abbott, "Managing the attractive magnetic force between an untethered magnetically actuated tool and a rotating permanent magnet," in *IEEE Int. Conf. Robotics and Automation*, 2013, pp. 5346–5351.
- [20] K. M. Popek, A. W. Mahoney, and J. J. Abbott, "Localization method for a magnetic capsule endoscope propelled by a rotating magnetic dipole field," in *IEEE Int. Conf. Robotics and Automation*, 2013, pp. 5328–5333.
- [21] A. J. Petruska and J. J. Abbott, "Optimal permanent-magnet geometries for dipole field approximation," *IEEE Trans. Magn.*, vol. 49, no. 2, pp. 811–819, 2013.
- [22] R. M. Murray, Z. Li, and S. S. Sastry, *A Mathematical Introduction to Robotic Manipulation*. CRC Press, Boca Raton, 1994.

CHAPTER 4

REMOTE MANIPULATION WITH A STATIONARY COMPUTER- CONTROLLED MAGNETIC DIPOLE SOURCE

The Omnimagnet, developed in the last chapter, is a stationary magnetic dipole-source and can generate controllable magnetic dipole fields. By choosing to control field primarily, or field gradients primarily, this paper demonstrates the capabilities of a single stationary dipole-source to control an adjacent object. It has been accepted for publication in IEEE Transactions on Robotics and is reproduced here with permission.

A. J. Petruska, A. W. Mahoney, and J. J. Abbott, “Remote manipulation with a stationary computer-controlled magnetic dipole source,” *IEEE Tran Robot*, vol. 30, no. 5, pp. 1–6, 2014

©2014 IEEE. Personal use of this material is permitted. Permission from IEEE must be obtained for all other uses, in any current or future media, including reprinting/republishing this material for advertising or promotional purposes, creating new collective works, for resale or redistribution to servers or lists, or reuse of any copyrighted component of this work in other works.

Short Paper

Remote Manipulation With a Stationary Computer-Controlled Magnetic Dipole Source

Andrew J. Petruska, Arthur W. Mahoney, and Jake J. Abbott

Abstract—In this paper, we examine several magnetic control methods that utilize the fully controllable dipole field generated by the single stationary dipole source. Since the magnetic field generated by a dipole source is nonuniform, it applies both forces and torques to magnetic objects and can be used to manipulate magnetic tools. Recently, the Omnimagnet, a computer-controlled magnetic dipole source capable of varying both its dipole-moment direction and magnitude, was developed to perform magnetic manipulation. The equations and methods are developed generally; therefore, they can be applied to any omnidirectional dipole source, but their effectiveness is demonstrated using the Omnimagnet.

Index Terms—Magnetic manipulation, medical robotics, microrobotics, omnimagnet, teleoperation.

I. INTRODUCTION

Manipulation systems typically require a mechanical connection between the tool and the actuation system to achieve a desired force or torque transfer. This connection is a limiting factor when controlling objects in areas with access restrictions such as minimally invasive surgery, in environments with imaging limitations where a mechanical connection can obscure the field of view, and in low-Reynolds-number fluid environments where a mechanical connection can result in significant environmental disturbances. Using combinations of electromagnets and permanent magnets, a controllable torque and force can be applied to a tool without having a mechanical connection. Fundamentally, there have been two design approaches for electromagnet systems in the past: engineer a field that is aligned in a desired direction with a controllable gradient in the same direction (e.g., MRI systems and Helmholtz with Maxwell coils [1]–[4]) or design a system that has a nonuniform field shape and then calibrate a model or look-up table for the system *in situ* [5]–[12]. Permanent-magnet-based systems have been designed to use follow-the-leader dragging and rotating control approaches, and they have demonstrated dexterous manipulation using the dipole-field model without calibration [8], [9], [13]–[16].

This paper explores the capabilities and limitations of performing magnetic manipulation with an omnidirectional dipole source using the dipole-field equations recently exploited for permanent-magnetic control. Many devices can be modeled as an omnidirectional dipole source at large distances (see, e.g., [5]). Recently, the authors designed the Omnimagnet, which is an omnidirectional electromagnetic source accurately modeled by a point-dipole field comprising three solenoids

with a spherical ferromagnetic core nested such that they share the same magnetic center [17]. The analysis in this paper is developed in a general framework allowing for multiple solenoids and non-Omnimagnet-specific equations, but all demonstrations will be performed with an Omnimagnet.

In this paper, we will use bold font to represent vectors (e.g., \mathbf{a} , \mathbf{A}) and capitalized blackboard font to represent matrices (e.g., \mathbb{B}). The two-norm of a vector will be expressed as $\|\mathbf{a}\|$, the inner product of two vectors will be expressed as $\mathbf{a} \cdot \mathbf{b}$, the cross product of two vectors will either be expressed as $\mathbf{a} \times \mathbf{b}$ or in the skew-symmetric matrix form $\mathbb{S}(\mathbf{a})\mathbf{b}$, the unit-length direction of a vector will be written as $\hat{\mathbf{a}}$, and the transpose of a vector or matrix will be expressed as \mathbf{a}^T .

II. MAGNETICS BACKGROUND

The magnetic field produced by a collection of electromagnets can be modeled with a series expansion, which is called a multipole expansion, if the region of interest is outside of the smallest sphere that encapsulates all of the magnetic sources (i.e., the bounding sphere). The first term in the multipole expansion is called the dipole field, and its magnitude decays with $\|\mathbf{p}\|^{-3}$, where \mathbf{p} is the vector that points from the center of the bounding sphere to the point of interest. The second term, which is called the quadrupole term, decays as $\|\mathbf{p}\|^{-5}$, and the higher order terms decay with monotonically increasing odd powers. By using the multipole expansion, it is possible to have an accurate representation of the magnetic field at distances far from the source (i.e., greater than 1.5 bounding-sphere radii) without having to use computationally intensive (e.g., numerical integration) or experimentally intensive (e.g., *in situ* calibration) techniques [18].

The dipole moment \mathbf{m} of an electromagnetic source when all integral ferromagnetic materials are unsaturated can be written as

$$\mathbf{m} = \mathbb{M}\mathbf{I} \quad (1)$$

where \mathbb{M} is a linear mapping of a column-vector packing of the applied currents \mathbf{I} to the resulting dipole moment \mathbf{m} ; the rank of \mathbb{M} must be three for magnetic omnidirectionality. The dipole field at any point \mathbf{p} , which is relative to the center of the source's bounding sphere, is given by the dipole-field equation:

$$\mathbf{B} = \frac{\mu_0}{4\pi \|\mathbf{p}\|^3} (3\hat{\mathbf{p}}\hat{\mathbf{p}}^T - \mathbb{I}) \mathbf{m} \quad (2)$$

where \mathbb{I} is a 3×3 identity matrix, and μ_0 is the magnetic permeability of free space [19].

This paper will focus on the manipulation of objects (or tools) that are well modeled by a dipole field, that is, objects that are several bounding-sphere radii away from the source. The tool's dipole moment will be represented as \mathbf{m}_t , and, in general, the force \mathbf{F} and torque \mathcal{T} acting on this object when placed in a magnetic field \mathbf{B} are given by [19]

$$\mathbf{F} = (\mathbf{m}_t \cdot \nabla) \mathbf{B} \quad (3)$$

$$\mathcal{T} = \mathbf{m}_t \times \mathbf{B} \quad (4)$$

where ∇ is the gradient operator.

III. FIELD CONTROL

Sensing Requirements: Position \mathbf{p} .

Limitations: If the desired field is changed rapidly, the system dynamics may not be able to keep up.

Manuscript received November 18, 2013; accepted February 12, 2014. This paper was recommended for publication by Associate Editor S. Régnier and Editor B. J. Nelson upon evaluation of the reviewers' comments. This work was supported by the National Science Foundation under Grant 0952718 and Grant 0654414.

A. J. Petruska and J. J. Abbott are with the Department of Mechanical Engineering, University of Utah, Salt Lake City, UT 84112 USA (e-mail: Andrew.Petruska@utah.edu; jake.abbott@utah.edu).

A. W. Mahoney is with the School of Computing, University of Utah, Salt Lake City, UT 84112 USA (e-mail: art.mahoney@utah.edu).

Color versions of one or more of the figures in this paper are available online at <http://ieeexplore.ieee.org>.

Digital Object Identifier 10.1109/TRO.2014.2340111

To determine the dipole moment \mathbf{m} required by the source to produce a desired field \mathbf{B} at some point \mathbf{p} , the vector dipole equation (2) must be inverted. Using the dipole field analysis in [15] and [19], it can be shown that the inverse exists of the form

$$\mathbf{m} = \frac{2\pi}{\mu_0} \|\mathbf{p}\|^3 (3\hat{\mathbf{p}}\hat{\mathbf{p}}^T - 2\mathbb{I}) \mathbf{B}. \quad (5)$$

Combining with (1), the currents required to generate a field are thus

$$\mathbf{I} = \frac{2\pi}{\mu_0} \|\mathbf{p}\|^3 \mathbb{M}^\dagger (3\hat{\mathbf{p}}\hat{\mathbf{p}}^T - 2\mathbb{I}) \mathbf{B} \quad (6)$$

where \dagger identifies a generalized inverse, as \mathbb{M} may not be square, and multiple solutions could exist.

When placed in a magnetic field, an unconstrained magnetic tool will align with the applied field because of the magnetic torque (4) experienced. If the field is rotating, the tool will attempt to keep up with the rotation as well. This tendency to align with the field has been explored using a rotating permanent magnet to propel a ball and helical screw [15]. To perform similar control tasks with a dipole source, the desired field \mathbf{B} in (6) should be rotated at a desired angular velocity ω , and the position should be updated with the tool position. By doing so, a rotating field that translates with the object will be produced and can be used for propulsion. The maximum achievable tool rotation speed $\|\omega_{\max}\|$ is limited by the maximum magnetic torque that can be achieved to counteract the drag torques. The maximum torque, from inspection of (4), is $\|\mathbf{m}_t\| \|\mathbf{B}\|$ and corresponds to the configuration where the tool's dipole moment is consistently orthogonal to the applied rotating field. Operating at a faster speed than this, without increasing the applied field strength, will cause the system to experience step out [1].

A rotating magnetic field generated by an Omnimaget was used to propel a threaded capsule-endoscope mockup down a transparent lumen in [17]. In that demonstration, helical propulsion through a lumen presented a convenient system for using rotating fields to propel an object because a lumen provides significant physical constraints on the tool's motion. However, these physical constraints are not required to propel an object using a rotating field. To explore using an Omnimaget for control of adjacent objects in a less constrained environment, a magnetic ball was driven on a flat surface using only position information and a rotating field. The position information was obtained with a vision system, and the drive currents were updated at 100 Hz. The results of driving the ball around a rectangular path on a tabletop and around a Labyrinth maze, shown, respectively, in Fig. 1(a) and (b), demonstrate the capability of the Omnimaget to control the strength and direction of a field at an arbitrary location in space. Unfortunately, it is possible for disturbances, such as attractive magnetic forces or surface roughness, to apply torques about the dipole moment that cannot be compensated magnetically. In the demonstrations, these disturbances cause the magnet to deviate from a straight trajectory.

Micromanipulation of objects using magnetic torque and force has been explored using multiple-magnet systems that surround the viewing workspace [20]–[22]. The Omnimaget can produce similar control of microbeads through rolling as demonstrated previously; however, the problem is greatly simplified. Since the micromanipulation workspace is constrained to be under a microscope for viewing, the workspace is necessarily small compared with the Omnimaget's workspace. As such, the position of the microdevice being manipulated can be assumed to be constant, and a rotating field can be applied in an open-loop fashion. Fig. 1(c) shows the manipulation of a 1-mm magnetic ball in a viscous medium. Using a Reynolds-number analysis, the 1-mm-diameter permanent-magnet sphere in corn syrup (2500 cP, $1.36 \text{ g} \cdot \text{ml}^{-1}$) has a behavior equivalent to a $30\text{-}\mu\text{m}$ sphere in water.

Note that the Omnimaget is offset from the workspace by a relatively large distance (150 mm), allowing for manipulation under a microscope with the Omnimaget placed as necessary to accommodate other equipment.

IV. TORQUE CONTROL

Sensing Requirements: Position \mathbf{p} and tool dipole moment \mathbf{m}_t .

Limitations: Torque can only be applied orthogonal to the tool's dipole moment.

If both the heading and position of the tool are known, it is possible to directly apply a torque. Because of the cross product in (4), no component of torque can be applied parallel to the dipole moment of the tool, reducing the space of achievable torques to those orthogonal to the tool's dipole moment. Thus, it is assumed that any desired torque \mathcal{T} lies in this reachable plane. For any \mathcal{T} , there is a 1-D subspace of solutions, parameterized by θ , for the required field and currents

$$\mathbf{B} = \frac{\|\mathcal{T}\|}{\|\mathbf{m}_t\|} (\cot(\theta)\hat{\mathbf{m}}_t + \hat{\mathcal{T}} \times \hat{\mathbf{m}}_t) \quad (7)$$

$$\mathbf{I} = \frac{2\pi\|\mathcal{T}\|\|\mathbf{p}\|^3}{\mu_0\|\mathbf{m}_t\|} \mathbb{M}^\dagger (3\hat{\mathbf{p}}\hat{\mathbf{p}}^T - 2\mathbb{I}) (\cot(\theta)\hat{\mathbf{m}}_t + \hat{\mathcal{T}} \times \hat{\mathbf{m}}_t). \quad (8)$$

The solution that corresponds to $\theta = \pi/2$ is the minimum-field solution. It represents the case where the applied field is perpendicular to the tool's dipole moment and has been shown to minimize the attractive force between the two dipoles [23].

In some configurations, it is possible to choose a solution that requires less electrical power than the one corresponding to the minimum-field solution and produce the same torque by allowing some field magnitude in the tool's dipole-moment direction and exerting additional force. Letting \mathbb{R} be the positive-definite diagonal matrix packing of the electrical resistance associated with each current, the electrical power required is $\mathbf{I}^T \mathbb{R} \mathbf{I}$. The currents required to produce a torque with minimum electrical power are

$$\mathbf{I} = \frac{4\pi\|\mathbf{p}\|^3}{\mu_0} \mathbb{R}^{-1/2} (\mathbb{S}(\mathbf{m}_t) (3\hat{\mathbf{p}}\hat{\mathbf{p}}^T - \mathbb{I}) \mathbb{M} \mathbb{R}^{-1/2})^\dagger \mathcal{T} \quad (9)$$

where \dagger in this solution is the Moore–Penrose generalized inverse. Alternatively, the unused degree of freedom (DOF) can be used to optimize other favorable parameters, such as minimizing the difference between the resulting force applied and some desired force or direction of motion.

V. FORCE CONTROL

Sensing Requirements: Position \mathbf{p} and tool dipole moment \mathbf{m}_t .

Limitations: A singularity exists when the tool's dipole moment is orthogonal to the position vector, reducing the space of achievable forces in this configuration to the plane spanned by the tool's dipole moment and the position vector.

To apply a controlled force for pushing and pulling tasks, the field gradient at the position of the tool must be controlled. The force between two magnetic dipoles can be expressed as [19]

$$\begin{aligned} \mathbf{F} &= \frac{3\mu_0}{4\pi\|\mathbf{p}\|^4} \mathbb{F} \mathbf{m} \\ \mathbb{F} &\equiv \mathbf{m}_t \hat{\mathbf{p}}^T + \hat{\mathbf{p}} \mathbf{m}_t^T + (\hat{\mathbf{p}} \cdot \mathbf{m}_t) (\mathbb{I} - 5\hat{\mathbf{p}}\hat{\mathbf{p}}^T). \end{aligned} \quad (10)$$

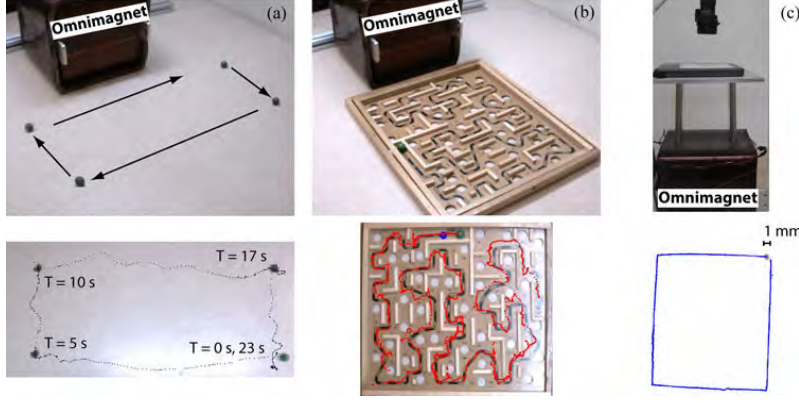


Fig. 1. Position control of a spherical magnet using a rotating field to direct the rolling direction of the ball. (a) 12.5-mm-diameter ball rolling without constraint on a plane adjacent to the Omnimagnet. (b) 12.5-mm diameter ball being directed through a Labyrinth maze adjacent to the Omnimagnet. (c) 1-mm diameter ball rolling in corn syrup on a plane above the Omnimagnet. In (a) and (b), the ball's position is found using computer vision and used in closed-loop control. In (c), the ball is controlled open loop under the assumption that it is always located in the center of the workspace.

Thus, the currents required to apply a particular force \mathbf{F} are

$$\mathbf{I} = \frac{4\pi}{3\mu_0} \|\mathbf{p}\|^4 \mathbb{M}^\dagger \mathbb{F}^{-1} \mathbf{F} \quad (11)$$

$$\mathbb{F}^{-1} = \frac{(2(\hat{\mathbf{p}} \cdot \mathbf{m}_t)^2 + \mathbf{m}_t \cdot \mathbf{m}_t) \mathbb{I} - \mathbb{F}^2}{(\hat{\mathbf{p}} \cdot \mathbf{m}_t)((\hat{\mathbf{p}} \cdot \mathbf{m}_t)^2 + \mathbf{m}_t \cdot \mathbf{m}_t)}.$$

The inverse of \mathbb{F} exists when the inner product of the tool's dipole moment \mathbf{m}_t and the displacement direction $\hat{\mathbf{p}}$ is nonzero.

When \mathbf{m}_t and $\hat{\mathbf{p}}$ are orthogonal, \mathbb{F} is singular, but forces can still be produced in the plane spanned by \mathbf{m}_t and $\hat{\mathbf{p}}$, and the currents necessary to command a desired force in this plane are

$$\mathbf{I} = \frac{4\pi \|\mathbf{p}\|^4}{3\mu_0 \|\mathbf{m}_t\|} \mathbb{M}^\dagger (\hat{\mathbf{m}}_t \hat{\mathbf{p}}^T + \hat{\mathbf{p}} \hat{\mathbf{m}}_t^T) \mathbf{F}. \quad (12)$$

In the singular configuration, any currents that contribute to a dipole moment not in the span of $\{\mathbf{m}_t, \hat{\mathbf{p}}\}$ create no force. The torque associated with a desired force in the singular configuration is

$$\mathcal{T} = 2(\mathbf{m}_t \cdot \mathbf{F}) \|\mathbf{p}\| (\hat{\mathbf{m}}_t \times \hat{\mathbf{p}}). \quad (13)$$

Therefore, it is possible to apply a torque or a force that would rotate or move the tool such that \mathbf{m}_t is no longer orthogonal to $\hat{\mathbf{p}}$, thereby restoring full force control. Since the direction of the field and the torque applied are not controlled, the resulting force solution will likely be locally rotationally unstable. Consequently, open-loop unconstrained force control with a single dipole source is not feasible in practice. However, if the tool's dipole moment is known, through sensing or mechanical support (e.g., a lumen), pushing and pulling an object using a dipole source with feedback is possible provided the singularity is avoided or appropriately mitigated.

To demonstrate this capability, an axially magnetized permanent magnet disk is fixed to a larger plastic disk, placed in a tub of water, and driven around a rectangular path (see Fig. 2). The buoyant forces on the plastic disk serve to constrain the tool's dipole moment to the vertical direction, and its location is tracked with a vision system. A closed-loop proportional-derivative position controller is used to determine the forces to apply, and (11) is used to convert these into the required electrical currents.

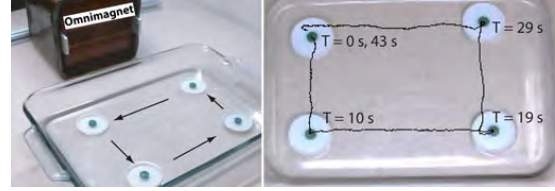


Fig. 2. Position servo control of a floating magnet using applied force, generated by an Omnimagnet [17]. The dipole moment of the magnet is constrained by buoyant forces to be in the vertical direction.

VI. FIELD-ALIGNED FORCE CONTROL

Sensing Requirements: Position \mathbf{p} and tool dipole magnitude $\|\mathbf{m}_t\|$. *Additional Assumptions:* The tool is aligned with the applied field.

Limitations: No repulsive forces can be applied to the tool, requiring nonmagnetic forces for system stability. The space of achievable magnetic forces is reduced to a 28° cone opening toward the dipole source. Rapid changes in force direction, relative to the tool's rotational time constant, will cause the tool to become misaligned with the field and the applied force to deviate from the desired force.

Field alignment of an unconstrained tool has been exploited previously for 5-DOF heading and force control [7], [16]. Although it is not possible to achieve 5-DOF control with a single stationary dipole source, 3-DOF force control can be achieved. The force applied to an adjacent magnetic tool from a dipole source when the tool is aligned with the source's field is

$$\mathbf{F} = \frac{3\mu_0 \|\mathbf{m}_t\|}{4\pi \|\mathbf{p}\|^4} \frac{((\hat{\mathbf{p}} \cdot \hat{\mathbf{m}}) \mathbf{m} - (4(\hat{\mathbf{p}} \cdot \hat{\mathbf{m}})^2 + 1) \|\mathbf{m}\| \hat{\mathbf{p}})}{\sqrt{3(\hat{\mathbf{p}} \cdot \hat{\mathbf{m}})^2 + 1}}. \quad (14)$$

If a ball with a large magnetic susceptibility were used instead of a permanent magnet, then $\|\mathbf{m}_t\|$ would be a function of the applied field

$$\|\mathbf{m}_t\| = \frac{3\mathcal{V}_b \|\mathbf{m}\|}{4\pi \|\mathbf{p}\|^3} \sqrt{3(\hat{\mathbf{p}} \cdot \hat{\mathbf{m}})^2 + 1} \quad (15)$$

where \mathcal{V}_b is the volume of the unsaturated magnetized ball.

Inspection of (14) shows that the force will always be attractive (i.e., there will always be a component in the $-\hat{\mathbf{p}}$ direction); thus, it is necessary to have an external restoring force (e.g., gravity) to stabilize the direction of attraction. By using the projections $\mathbf{F} \cdot \hat{\mathbf{p}}$ and $\mathbf{F} \cdot \mathbf{F}$, it is possible to obtain a closed-form solution for the required dipole-moment to achieve a desired force

$$\mathbf{m} = \pm \frac{4\pi \|\mathbf{p}\|^4}{3\mu_0 \|\mathbf{m}_t\|} \sqrt{\frac{3(\hat{\mathbf{p}} \cdot \hat{\mathbf{m}})^2 + 1}{(\hat{\mathbf{p}} \cdot \hat{\mathbf{m}})^2}} \left(\mathbb{I} - \left(\frac{4(\hat{\mathbf{p}} \cdot \hat{\mathbf{m}})^2 + 1}{3(\hat{\mathbf{p}} \cdot \hat{\mathbf{m}})^2 + 1} \right) \hat{\mathbf{p}} \hat{\mathbf{p}}^T \right) \mathbf{F} \quad (16)$$

where $(\hat{\mathbf{p}} \cdot \hat{\mathbf{m}})^2$ is given by

$$(\hat{\mathbf{p}} \cdot \hat{\mathbf{m}})^2 = \frac{7(\hat{\mathbf{F}} \cdot \hat{\mathbf{p}})^2 - 6 \pm (\hat{\mathbf{F}} \cdot \hat{\mathbf{p}}) \sqrt{17(\hat{\mathbf{F}} \cdot \hat{\mathbf{p}})^2 - 16}}{18 - 16(\hat{\mathbf{F}} \cdot \hat{\mathbf{p}})^2}. \quad (17)$$

The magnitude of \mathbf{m} is always

$$\|\mathbf{m}\| = \frac{4\pi \|\mathbf{p}\|^4}{3\mu_0 \|\mathbf{m}_t\|} \sqrt{\frac{-(\mathbf{F} \cdot \hat{\mathbf{p}})}{3(\hat{\mathbf{p}} \cdot \hat{\mathbf{m}})^2 + 1}}. \quad (18)$$

When a solution exists, (16) provides four choices of \mathbf{m} that will apply the same force—two directions, each in the positive or negative sense. In the special case when $\hat{\mathbf{F}} \cdot \hat{\mathbf{p}} = 1$, one solution for $\hat{\mathbf{p}} \cdot \hat{\mathbf{m}}$ is 0 corresponding to the force singularity. In this configuration, (16) no longer yields a solution for the dipole moment; however, there exists an infinite number of solutions corresponding to dipole moments in the plane defined by $\hat{\mathbf{p}} \cdot \hat{\mathbf{m}} = 0$ with a magnitude given by (18).

Together, (17) and (18) define a geometric constraint on what force directions can be achieved when the tool is aligned with the dipole field:

$$\hat{\mathbf{F}} \cdot \hat{\mathbf{p}} \leq -\sqrt{\frac{16}{17}}. \quad (19)$$

This constraint requires any applied force to be attractive (i.e., have a component in the $-\hat{\mathbf{p}}$ direction), and confines an applied force direction to differ from the $\hat{\mathbf{p}}$ direction by no more than $\arccos(\sqrt{16/17}) \approx 14^\circ$, and, thus, constrains the workspace of the tool to a 28° cone emanating from the center of the dipole source and directed along the direction of the restoring force. Without loss of generality, we will assume for the remainder of this discussion that the restoring force is gravity, that it acts in the $-\hat{\mathbf{z}}$ Cartesian direction, and that the dipole source is located at the origin.

To discuss the manipulability of a tool in this framework, it is useful to switch to a cylindrical coordinate frame where the axis of the cylinder is aligned with the $\hat{\mathbf{z}}$ -direction, and the radial and circumferential directions describe motion in a horizontal plane below the dipole source. The location of a tool will be defined by $(z\hat{\mathbf{z}}, r\hat{\mathbf{r}}, \phi\hat{\boldsymbol{\phi}})$, but because of symmetries in the dipole field, only the z and r values will affect the following discussion. In this framework, the angle $\theta = \arctan(r/z)$ will describe where in the conic workspace the tool is operating.

In the achievable workspace, $\hat{\mathbf{p}}$ will always have its largest component in the $-\hat{\mathbf{z}}$ -direction (i.e., the restoring force direction), and (19) further requires the largest component of any achievable force to be in the $+\hat{\mathbf{z}}$ -direction. Therefore, it is convenient to normalize any applied horizontal force with the applied vertical force with the understanding that as the applied vertical force is reduced to zero, any horizontal components must also go to zero. Fig. 3 shows how the space of achievable radial and circumferential forces changes as the tool moves from being positioned directly under the source ($r = 0 \Leftrightarrow \theta = 0^\circ$) to being

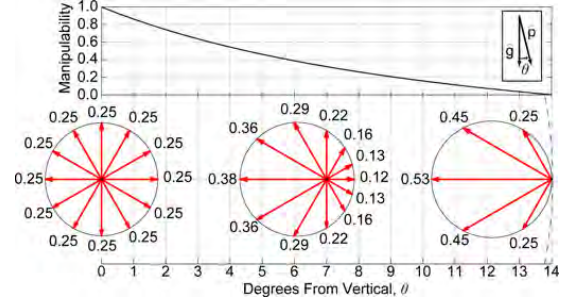


Fig. 3. (Top) Manipulability measure of a tool aligned with a source's dipole field as a function of angular position inside of the 28° conic workspace. The manipulability is the ratio of minimum to maximum force that can be applied to the tool in the horizontal plane by the source. (Bottom) Achievable forces at three locations from the center ($\theta = 0^\circ$) to the edge ($\theta = 14^\circ$) of the cone. The magnitude of these forces are normalized by the applied vertical force; as the vertical force tends to zero, the horizontal forces must also go to zero. As the tool moves away from vertical alignment ($\theta = 0^\circ$), larger forces can be generated to push it toward $\theta = 0^\circ$ than to push it toward the edge of the workspace.

positioned at the edge of the conic workspace ($r = z/4 \Leftrightarrow \theta \approx 14^\circ$). The manipulability measure in the figure is defined as the minimum horizontal force (which is always in the positive radial direction) normalized by the maximum horizontal force (which is always in the negative radial direction). As the tool moves toward the boundary, the manipulability measure goes to zero because the achievable forces in both the circumferential and the positive radial directions go to zero.

Unfortunately, the geometric force constraint (19) prevents general application of (16). To implement a controller with this method, it is necessary to determine the set of achievable forces and then pick an achievable force that yields, as close as possible, the response required by the control system. As before, it is beneficial to split the desired force into a component parallel to the restoring force and one perpendicular to the restoring force: $\mathbf{F} = F_z \hat{\mathbf{z}} + \mathbf{F}_\perp$. For \mathbf{F} to be achievable, F_z must be positive, and $\|\mathbf{F}_\perp\|$ must be small enough to satisfy (19). The maximum achievable $\|\mathbf{F}_\perp\|$ can be found by finding a positive value of α , where

$$\mathbf{F} = F_z \hat{\mathbf{z}} + \alpha \hat{\mathbf{F}}_\perp \quad (20)$$

which satisfies (19) at the constraint boundary. This yields a quadratic equation for α

$$\left((\hat{\mathbf{p}} \cdot \hat{\mathbf{F}}_\perp)^2 - \frac{16}{17} \right) \alpha^2 + 2F_z ((\hat{\mathbf{p}} \cdot \hat{\mathbf{z}})(\hat{\mathbf{p}} \cdot \hat{\mathbf{F}}_\perp)) \alpha + F_z^2 \left((\hat{\mathbf{p}} \cdot \hat{\mathbf{z}})^2 - \frac{16}{17} \right) = 0. \quad (21)$$

Thus, the dipole moment that should be applied given a desired force and a restoring-force direction requires that \mathbf{F} in (16) and (17) be $F_z \hat{\mathbf{z}} + \min(\|\mathbf{F}_\perp\|, \alpha) \hat{\mathbf{F}}_\perp$, where α is the positive real solution to (21). If a positive and real solution for α exists, and if $\alpha \geq \|\mathbf{F}_\perp\|$, then the desired force can be achieved; otherwise, if $\alpha < \|\mathbf{F}_\perp\|$, then the desired force in the perpendicular direction cannot be achieved and must be reduced to have a magnitude of α . If no positive solution for α exists, then it is not possible to apply a force in the positive $\hat{\mathbf{F}}_\perp$ direction, which happens at the edge of the achievable workspace. If no real solution exists, then it is not possible to achieve $F_z \hat{\mathbf{z}}$ at this location, which happens if the position is outside of the achievable workspace.

A semiboyant capsule was levitated and driven along a rose curve using this field-aligned force control approach, as shown in Fig. 4,

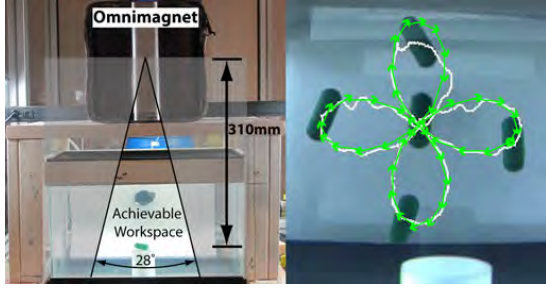


Fig. 4. Semiboyant capsule is levitated and position controlled about a rose curve using a field-aligned force control approach. The achievable workspace is confined to the 28° cone shown.

using a proportional-derivative controller with visual tracking at a 30-Hz update rate. The orientation of the capsule shows the applied field direction required at each snapshot to achieve the control forces. If the manipulated tool were a sphere, the uncontrolled orientation would not be seen. The capsule has larger tracking error closer to the Omnimagnet; this is likely because the assumption that the Omnimagnet's field is a pure dipole field has more error close to the Omnimagnet, with the error reducing with $\|\mathbf{p}\|^{-7}$ [17]. The tracking error could be reduced by moving the trajectory farther from the Omnimagnet.

VII. COMMENT ON REFLECTIVE FORCE AND TORQUE

Because the Omnimagnet used in these demonstrations contains a spherical ferromagnetic core, the permanent magnet used in a magnetic tool will slightly magnetize the core, causing the permanent magnet to be slightly attracted to the Omnimagnet even when no power is applied. Assuming the permanent-magnet tool can be modeled as a point dipole, which is reasonable for relatively large separation distances [18], the dipole moment of the soft-magnetic core, \mathbf{m}_c , due to the permanent magnet, \mathbf{m}_t , can be determined by the method provided in [17]

$$\mathbf{m}_c = \frac{R_c^3}{\|\mathbf{p}\|^3} (3\hat{\mathbf{p}}\hat{\mathbf{p}}^T - \mathbb{I}) \mathbf{m}_t \quad (22)$$

where R_c is the radius of the core. The torque and force on the magnetic tool due to the reflection are

$$\mathcal{T} = \frac{3\mu_0 R_c^3}{4\pi\|\mathbf{p}\|^6} (\hat{\mathbf{p}} \cdot \mathbf{m}_t)(\mathbf{m}_t \times \hat{\mathbf{p}}) \quad (23)$$

$$\mathbf{F} = -\frac{3\mu_0 R_c^3 \|\mathbf{m}_t\|^2}{4\pi\|\mathbf{p}\|^7} (3\hat{\mathbf{m}}_t \hat{\mathbf{m}}_t^T + \mathbb{I}) \hat{\mathbf{p}}. \quad (24)$$

For perspective, if a 1-cm³ NdFeB grade-N52 magnet, which has a dipole moment of 1.17 A · m², is placed at the surface of the outer coil of an Omnimagnet with the same geometry as the one used in the experiments, the maximum torque would be 59×10^{-3} mN · m, and the maximum force would be 5.3 mN (only 7% of its weight). To account for this coupling, the Omnimagnet's solenoid currents can be controlled such that the net dipole moment of the Omnimagnet becomes zero by using (1) to calculate the currents required to create a dipole moment that is the negative of (22) and, then, adding that quantity to whatever dipole moment is required for the task. This adjustment was not necessary in the above demonstrations because of the relatively low reflective torques and forces at the operation distances of the demonstrations, and because of the closed-loop controllers used. However, since the reflective torque and force scales with the square

of the tool's dipole moment, this effect could become significant for magnetically stronger tools. Although this analysis assumes a spherical core, the scaling will be similar for dipole sources that contain nonspherical ferromagnetic elements.

VIII. CONCLUSION

A single stationary electromagnetic dipole source can be used to manipulate adjacent tools using several methods. If both the position and heading of the tool are known or sensed, direct force and torque control methods can be applied. If only position information is available, in many instances, it is possible to assume the tool will attempt to align with the applied field, enabling both rotating-field control and field-aligned force control approaches. Unfortunately, the workspace for field-aligned force control is fairly limited. Many demonstrations in this paper are conducted in 2-D workspaces, e.g., ball rolling; however, the methods developed for manipulation with a single controlled source are equally applicable to general 3-D workspaces under the provided assumptions.

REFERENCES

- [1] K. Ishiyama, M. Sendoh, A. Yamazaki, and K. I. Arai, "Swimming micro-machine driven by magnetic torque," *Sens. Actuators A*, vol. 91, pp. 141–144, 2001.
- [2] K. B. Yesin, K. Vollmers, and B. J. Nelson, "Modeling and control of untethered biomicrobots in a fluidic environment using electromagnetic fields," *Int. J. Robot. Res.*, vol. 25, nos. 5/6, pp. 527–536, 2006.
- [3] J. B. Mathieu, G. Beaudoin, and S. Martel, "Method of propulsion of a ferromagnetic core in the cardiovascular system through magnetic gradients generated by an MRI system," *IEEE Trans. Biomed. Eng.*, vol. 53, no. 2, pp. 292–299, Feb. 2006.
- [4] S. Jeon, G. Jang, H. Choi, and S. Park, "Magnetic navigation system with gradient and uniform saddle coils for the wireless manipulation of micro-robots in human blood vessels," *IEEE Trans. Magn.*, vol. 46, no. 6, pp. 1943–1946, Jun. 2010.
- [5] M. Grady, M. Howard III, J. Molloy, R. Ritter, E. Quate, and G. Gillies, "Nonlinear magnetic stereotaxis: Three-dimensional, in vivo remote magnetic manipulation of a small object in canine brain," *Med. Phys.*, vol. 17, pp. 405–415, 1990.
- [6] D. Meeker, E. H. Maslen, R. C. Ritter, and F. Creighton, "Optimal realization of arbitrary forces in a magnetic stereotaxis system," *IEEE Trans. Magn.*, vol. 32, no. 2, pp. 320–328, Mar. 1996.
- [7] M. P. Kummer, J. J. Abbott, B. E. Kratochvil, R. Borer, A. Sengul, and B. J. Nelson, "OctoMag: An electromagnetic system for 5-DOF wireless micromanipulation," *IEEE Trans. Robot.*, vol. 26, no. 6, pp. 1006–1017, Dec. 2010.
- [8] M. H. Hagiwara, T. K. Kawahara, Y. Yamanishi, and F. Arai, "Driving method of microtool by horizontally arranged permanent magnets for single cell manipulation," *Appl. Phys. Lett.*, vol. 97, pp. 013701-1–013701-3, 2010.
- [9] G. Ciuti, P. Valdastrì, A. Menciassi, and P. Dario, "Robotic magnetic steering and locomotion of capsule endoscope for diagnostic and surgical endoluminal procedures," *Robotica*, vol. 28, no. 2, pp. 199–207, 2010.
- [10] M. Mehrtash and M. B. Khamesee, "Design and implementation of LQG/LTR controller for a magnetic telemanipulation system: performance evaluation and energy saving," *Microsyst. Technol.*, vol. 17, no. 5–7, pp. 1135–1143, 2011.
- [11] A. Komae and B. Shapiro, "Steering a ferromagnetic particle by optimal magnetic feedback control," *IEEE Trans. Control Syst. Technol.*, vol. 20, no. 4, pp. 1011–1024, Jul. 2012.
- [12] P. Berkelman and M. Dzadovsky, "Magnetic levitation over large translation and rotation ranges in all directions," *IEEE/ASME Trans. Mechatronics*, vol. 18, no. 1, pp. 44–52, Feb. 2013.
- [13] M. Simi, G. Sardi, P. Valdastrì, A. Menciassi, and P. Dario, "Magnetic levitation camera robot for endoscopic surgery," in *Proc. IEEE Int. Conf. Robot. Autom.*, 2011, pp. 5279–5284.
- [14] A. W. Mahoney and J. J. Abbott, "Managing magnetic force applied to a magnetic device by a rotating dipole field," *Appl. Phys. Lett.*, vol. 99, pp. 134103-1–134103-3, 2011.

- [15] A. W. Mahoney and J. J. Abbott, "Generating rotating magnetic fields with a single permanent magnet for propulsion of untethered magnetic devices in a lumen," *IEEE Trans. Robot.*, vol. 30, no. 2, pp. 411–420, Apr. 2014.
- [16] A. W. Mahoney and J. J. Abbott, "5-DOF manipulation of a magnetic capsule in fluid using a single permanent magnet: Proof-of-concept for stomach endoscopy," in *Proc. Hamlyn Symp. Med. Robot.*, 2013, pp. 114–115.
- [17] A. J. Petruska and J. J. Abbott, "Omnimagnet: An omnidirectional electromagnet for controlled dipole-field generation," *IEEE Trans. Magn.*, vol. 50, no. 7, p. 8400810, Jul. 2014.
- [18] A. J. Petruska and J. J. Abbott, "Optimal permanent-magnet geometries for dipole field approximation," *IEEE Trans. Magn.*, vol. 49, no. 2, pp. 811–819, Feb. 2013.
- [19] D. J. Griffiths, *Introduction to Electrodynamics*. Englewood Cliffs, NJ, USA: Prentice-Hall, 1999.
- [20] M. Gauthier and E. Piat, "Control of a particular micro-macro positioning system applied to cell micromanipulation," *IEEE Trans. Autom. Sci. Eng.*, vol. 3, no. 3, pp. 264–271, Jul. 2006.
- [21] C. Pawashe, S. Floyd, and M. Sitti, "Modeling and experimental characterization of an untethered magnetic micro-robot," *Int. J. Robot. Res.*, vol. 28, no. 8, pp. 1077–1094, 2009.
- [22] L. Zhang, J. Abbott, L. Dong, B. Kratochvil, D. Bell, and B. Nelson, "Artificial bacterial flagella: Fabrication and magnetic control," *Appl. Phys. Lett.*, vol. 94, pp. 064107-1–064107-3, 2009.
- [23] A. W. Mahoney, S. E. Wright, and J. J. Abbott, "Managing the attractive magnetic force between an untethered magnetically actuated tool and a rotating permanent magnet," in *Proc. IEEE Int. Conf. Robot. Autom.*, 2013, pp. 5346–5351.

CHAPTER 5

RECOMMENDATIONS FOR FUTURE WORK

A single Omnimagnet, with three independent control inputs, is limited to 3-dof control; multiple Omnimagnets, used in concert, will not share this fundamental limitation. The ferromagnetic cores in a system of Omnimagnets will magnetically couple all of the Omnimagnets together. Other electromagnet systems account for this coupling with *in situ* calibration or extensive FEA modeling. Unlike the other systems, the coupling in an Omnimagnet system can be solved analytically because of the unique properties of the spherical core; namely, the average field experienced by the core is equal to the field at the center of the core [1]. The magnetization of each Omnimagnet's core due to all of the Omnimagnets' currents can be computed in an analogous way to the methods in Chapter 3 for determining the magnetization of the core initially. This leads to a linear set of equations that relate how the current density in one coil affects the dipole moment of every Omnimagnet. Once this mapping is established, it is possible to solve for the net field of the system given the applied currents. As this is an analytical mapping, it will be possible to update the model in real-time, allowing for a dynamically reconfigurable system.

A multiple Omnimagnet system will have at least six control inputs, making it potentially capable of controlling the magnetic field gradient at a point independently from the local field at that point. This will enable 5-dof control of magnetic tools. Once the system has three or more Omnimagnets, the number of control inputs will exceed the number of controllable outputs, the system will be overactuated, and there will be multiple current combinations capable of generating the desired output. This overactuation can be exploited to minimize different objective functions such as the norm of the dipole moments, the electrical power consumed, or the coil temperatures. Although each of these choices will result in the same desired output, the realization of each system may have different performance characteristics once nonmagnetic constraints are introduced, e.g.,

current limits, power limits, and thermal limits. It is conceivable that different objective functions may be desirable while operating in different task modes.

Many magnetic manipulation tasks fundamentally have different stages. In a catheter ablation task, for example, the ablative end of the catheter must be steered through the tortuous network of blood vessels before it can be used to thermally ablate the undesirable tissue. These two subtasks, steering and ablation, fundamentally have different control needs. Steering primarily requires control of the torques applied at the end of the catheter (to turn right or left at a junction), while ablation primarily requires control of the forces applied at the end of the catheter (to press firmly into the wall for good thermal contact). Independently, these two modes of operation will have different optimal Omnimagnet configurations—one optimized for field control and one optimized for force control. Moreover, the optimal configuration for each mode of operation will change as the location and orientation of the catheter changes. Understanding how to reconfigure a system of Omnimagnets in real-time will provide a magnetic manipulation system that is more versatile and more efficient than a system that has been designed as a continual compromise.

Imaging during medical procedures is of equal importance to device manipulation. Many medical imaging systems, e.g., C-arm fluoroscopy, require line of sight and access to both sides of the patient. Using a static manipulation system with this imaging technology will significantly reduce the available imaging options. A dynamically reconfigurable manipulation system, however, could be repositioned during procedures to accommodate the needs of the imaging system allowing for potentially better imaging and diagnosis.

Because the field can be analyzed analytically, without the need of computationally expensive FEA simulations, it is possible to rapidly analyze Omnimagnet configurations, enabling high level real-time task replanning. During a magnetic manipulation task, there are many sources of uncertainty: e.g., the location and orientation of the tool, the exact field applied, and the interaction between the tool and the environment. Partially observable Markov decision processes analysis could be used to optimize not only the control currents applied to the Omnimagnets, but also the Omnimagnet positions during the procedure and the imaging orientations, maximizing the probability of success for any given task.

A single, movable, permanent-magnet source has been used to perform 5-dof control of a semibuoyant capsule [2]. This approach assumes that the dipole moment magnitude of the source cannot vary, making the system fully constrained (5-dof in actuation input and output). Using an Omnimagnet to perform similar control tasks would yield an

additional degree of freedom—the magnitude—making the system overactuated. Currently, the permanent-magnet system cannot control the strength of the applied field, only its direction, which makes it unsuitable for control of soft-magnetic end-effectors. Since a mobile Omnimagnet can have control of its dipole strength, controlling the field magnitude as well as direction is possible; thus, a single mobile Omnimagnet should be capable of performing state of the art control of a soft ferromagnetic ellipsoid demonstrated by the OctoMag system [3], but with fewer control inputs.

Commercially available permanent magnets have approximate dipole-moment densities of 2×10^6 A/m, whereas the optimal Omnimagnet design, assuming a maximum current density of 500 A/cm² (6.5 A in a 16 AWG conductor), has a dipole-moment density of only $3L \times 10^5$ A/m (where L is the edge length of the Omnimagnet). Thus, a permanent magnet of reasonable size will be 10 to 1000 times stronger than an equivalently sized Omnimagnet. For this reason, it may be desirable to use large permanent-magnet systems, or superconducting electromagnetic systems, to produce a strong quasi-static field while a faster responding Omnimagnet subsystem performs real-time micro adjustment of the field for control or other purposes.

The above research areas all focus on using the Omnimagnets as a manipulation field source; however, there is no reason to limit the Omnimagnet to a source device. A multiple Omnimagnet system will apply forces and torques between each Omnimagnet in the system. This could be exploited for formation flight systems in minimum gravity environments or actively controlled end-effectors in tethered operation. If a small Omnimagnet were placed at the distal end of a catheter, a large permanent magnet, like the Stereotaxis system [4], could generate a static field, while the Omnimagnet's dipole moment could be selected to obtain the desired forces and torques given that field. This approach could increase the dexterity for steering the catheter and also provide a heat source for ablation procedures.

Many of these applications require knowledge of the relative positions of all of the Omnimagnets. Omnimagnets are dynamic magnetic field sources, and there is no physical feature that prevents them from also performing as antennas. It should be possible to have each Omnimagnet broadcast a high-frequency signal, one that is much faster than the controlled device's dynamic response, and simultaneously listen for other Omnimagnet's signals in order to determine their relative positions in a similar manner to current magnetic localization systems. Moreover, it could also be possible to extract the position of the end-effector based on its electromagnetic effect on this high-frequency network.

5.1 References

- [1] D. J. Griffiths, *Introduction to Electrodynamics*. Upper Saddle River, NJ: Prentice Hall, 1999.
- [2] A. W. Mahoney and J. J. Abbott, “5-DOF manipulation of a magnetic capsule in fluid using a single permanent magnet: proof-of-concept for stomach endoscopy,” *Hamlyn Symp. Medical Robotics*, 2013.
- [3] M. P. Kummer, J. J. Abbott, B. E. Kratochvil, R. Borer, A. Sengul, and B. J. Nelson, “OctoMag: an electromagnetic system for 5-DOF wireless micromanipulation,” *IEEE Trans. Robot.*, vol. 26, no. 6, pp. 1006–1017, 2010.
- [4] S. Ernst, F. Ouyang, C. Linder, K. Hertting, F. Stahl, J. Chun, H. Hachiya, D. Bänsch, M. Antz, and K.-H. Kuck, “Initial experience with remote catheter ablation using a novel magnetic navigation system magnetic remote catheter ablation,” *Circulation*, vol. 109, no. 12, pp. 1472–1475, 2004.

CHAPTER 6

CONCLUSIONS

Using magnetic forces and torques to manipulate medical devices could revolutionize minimally invasive medicine. Current approaches for this type of magnetic manipulation system include using permanent magnets, which are dynamically oriented, or electromagnets, which are current controlled. Dexterous control with permanent-magnet systems have successfully used the dipole-field model for magnetic analysis, and electromagnet systems can be analyzed in a similar way. Unfortunately, the dipole-field model is only an approximation for most geometries, so understanding this approximation's limitations was the first step in the manipulation system design.

The dipole-field model is the first nonzero term in the multipole expansion and becomes increasingly accurate with increasing distances from the magnet. By minimizing the second nonzero term (the quadrupole term), it is possible to optimize an arbitrary shape for the dipole-field model. This optimization was carried out on several commercially available shapes, including a cylinder, a cuboid, and a washer. It was found that the optimal geometry for cylinders (both axially and diametrically magnetized) is a diameter-to-length ratio of $\sqrt{4/3}$ and for rectangular-cross-section bars is a cube. By choosing these ratios, the error associated with the dipole model is reduced compared to nonoptimal geometries as shown by the trend depicted in Fig. 2.6. The accuracy of the approximation increases faster with distance for optimal geometries than it does for nonoptimal geometries, and of the geometries studied for a given distance from the magnet, the cubic magnet has the least average dipole approximation error.

The multipole expansion can also be applied to electromagnets. As the optimal non-spherical shape in permanent magnets for a dipole-field model was the cube, a cubic shape for the electromagnet was chosen. The thickness and lengths of the windings were optimized to produce a field with no quadrupole moment and to generate equal strength per applied current in any direction, while the diameter of the core was chosen to maximize the

strength of the final design. The realized version of the design has an optimal core-radius to outer-length ratio of 0.57 and can achieve field strengths that are 87% of the unrealizable theoretical reference. The design was optimized to create a dipole-like field with the error relative to the dipole model falling to below 5% outside of 1.5 minimum-bounding-sphere radii from the center. Not only can the device create a rotating dipole field like a permanent magnet, but it can also control the field strength like a standard electromagnet.

Having constructed an electromagnetic dipole source, object manipulation could be explored. If both the position and heading of the tool are known or sensed, direct force and torque control methods can be applied. If only position information is available, in many instances it is possible to assume the tool will attempt to align with the applied field, enabling both rotating-field control and field-aligned force control approaches. Unfortunately, the workspace for field-aligned force control is fairly limited, which suggests that future research should examine how multiple dipole sources can be used for control.

The potential for use of multiple dipole sources for control is exciting. The choice of using a spherical core in the dipole source will enable analytical analysis of the coupled fields and could lead to the first real-time reconfigurable magnetic manipulation system. Furthermore, these sources could be used in conjunction with permanent-magnet systems to become the first hybrid system. This dissertation has presented the design and use of an electromagnetic device optimized for control approaches based on the dipole-field model, and potentially provides a foundation for future research into reconfigurable magnetic manipulation.